Linearly varying ambient flow past a sphere at finite Reynolds number. Part 1: wake structure and forces in steady straining flow

By P. BAGCHI
AND S. BALACHANDAR

Department of Theoretical and Applied Mechanics, University of Illinois at Urbana-Champaign, Urbana, IL 61801, USA

This study focuses on the effect of spatial non-uniformity in the ambient flow on the forces acting on a spherical particle at moderate particle Reynolds numbers. A scaling analysis is performed to obtain conditions under which such effects are important. A direct numerical simulation, based on spectral methods, is used to compute three-dimensional time-dependent flow past a stationary sphere subject to a uniform flow plus a planar straining flow. The particle Reynolds number, Re, in the range 10 to 300 covering different flow regimes, from unseparated flow to unsteady vortex shedding is considered. A variety of strain magnitudes and orientations are investigated. A systematic comparison with the potential flow results and axisymmetric strain results is given. Under elogational strain, both planar and axisymmetric cases are found to stabilize the sphere wake and delay onset of unsteadiness, while compressional strain leads to instability. In terms of separation angles, length of the recirculation eddy and topology of the surface streamlines, planar and axisymmetric strains yield nearly the same results. The drag force appears to have a linear relation with strain magnitude in both cases, as predicted by the potential flow. However, contrary to the potential flow results, the drag in planar strain is higher than that in axisymmetric strain. Generation of higher drag is explained using surface pressure and vorticity distribution. Planar strain oriented at an angle with the oncoming unform flow is observed to break the symmetry of the wake and results in a lift or side force. Variation of the drag and lift forces may be quite complex and unlike the potential flow results, they may not be monotonic with strain magnitude. The direction of the lift force may be opposite to that predicted by the inviscid and low Reynolds number ($Re \ll 1$) theories. This behavior is dictated by the presence or absence of a recirculation eddy. In the absence of a recirculation region at low Reynolds numbers ($Re < 20$), or, at a very high strain magnitude when the recirculation region is suppressed, results somewhat follow the pattern observed in potential flow. However, with the presence of a recirculation region, results opposite to those predicted by the potential theory are observed.

1. Introduction

Prediction of forces acting on a particle moving in a fluid is important in many particle-laden flows. Though the problem has received attention for nearly a century, many questions still remain unresolved. In particular, a generalized form for the equation of motion of an individual particle that allows for both temporal and spatial variations in the surrounding flow is still lacking. The effect of temporal acceleration in both the surrounding flow as well as of the particle itself has been investigated in great detail over the past years, especially in the context of low Reynolds number and potential flows and to some extent for finite particle Reynolds numbers. On the other hand, investigations of the effect of spatial non-uniformity in the undisturbed flow have been

primarily limited to potential flow and low Reynolds number limits. When the particle Reynolds number becomes finite, very little information is available as to the nature of the flow field and the resulting forces.

One of the earliest to recognize the importance of spatial non-uniformity in the undisturbed ambient flow on the motion of a particle is Taylor (1928), who was concerned with the motion of large airships. Taylor and later Tollmien (1938) computed the rate of change of kinetic energy of the fluid around bodies in irrotational non-uniform flows. Their investigations showed that the added-mass force acting on a stationary sphere in a steady straining flow is proportional to the pressure gradient measured at the center of the sphere. Taylor also performed wind tunnel experiments to confirm the inviscid theory in predicting the correct equilibrium position of bodies of different shapes in converging, diverging and curved flows. Over the years Taylor's work has been revisited and generalized by others including Voinov, Voinov & Petrov (1973), Auton (1987) and Auton, Hunt & Prud'homme (1988).

In the limit of zero Reynolds number, a generalization to the classical Basset-Boussinesq-Oseen (BBO) equation that incorporates the unsteady effect in the ambient flow was derived by Maxey & Riley (1983). In the Stokes flow regime velocity shear does not produce a lift force. However, quadratic variation in the ambient flow influences the force on the particle, and the effect of velocity curvature appears as the Faxen correction. At small but non-zero particle Reynolds numbers, even a linear variation in the undisturbed ambient flow may have a significant impact. The classic example is the lift force in a linear shear flow. Saffman (1965, 1968) obtained an expression for the lift force under the condition that $Re \ll \sqrt{Re_\sigma} \ll 1$, where $Re = \rho_f |\mathbf{U}_r| d/\mu$ is the particle Reynolds number, $\mathbf{U}_r$ measures the relative velocity of the flow with respect to the particle, $Re_\sigma = \sigma d^2 \rho_f / \mu$ is the shear Reynolds number, σ is the shear magnitude, d is the particle diameter, ρ_f and μ are the fluid density and viscosity. Over the years, Saffman's work has been extended in several significant ways by Harper & Chang (1968), Miyazaki, Bedeaux & Avalos (1995) and many others. McLaughlin (1991) extended Saffman's analysis on linear shear flow to situations where Re is not small compared to Re_σ. Analytical results were also obtained for wall-bounded shear flows by Schonberg & Hinch (1989), McLaughlin (1993), Hogg (1994) and Asmolov (1999). An interesting review on the subject is given by Stone (2000).

A variety of linearly varying ambient flows other than shear have also received attention in the limit of small but non-zero Re. For example, Herron, Davis & Bretherton (1975) and Weisenborn (1985) obtained expressions for force on a particle subjected to a pure rotational flow. Force due to a pure straining flow was obtained by Bedeaux and Rubi (1987) using the method of induced forces. Later Pérez-Madrid, Rubi & Bedeaux (1990) derived a general expression for force due to a combination of rotational and straining flows.

Investigation of the effects of non-uniform ambient flow at moderate Re ($\gtrsim 1$) has been limited. In most two-phase flow simulations, such effects are not taken into consideration due to the introduction of additional parameters as well as significantly increased cost of computation. Hence, the results of uniform ambient flow are taken for granted. This approach is indeed correct for particles of size much smaller than the smallest relevant flow scale, such as the Kolmogorov length scale, such that the ambient flow variation over one particle diameter is much smaller than the relative velocity $\mathbf{U}_r$. However, as the flow variation over a particle diameter becomes comparable to $\mathbf{U}_r$, the effect cannot be ignored. Numerical simulations of Magnaudet, Rivero & Fabre (1995) for axisymmetric straining flow and of Dandy & Dwyer (1990) and Kurose & Komori (1999) for linear shear flow showed that even a 10% variation in the ambient flow over a particle diameter can have significant effect. As in the previous investigations, in this paper also we will restrict attention to linearly varying flows. In other words, the undisturbed flow $\mathbf{U}(\mathbf{x})$ is expanded only up to $\nabla\mathbf{U}$ such that $\mathbf{U}(\mathbf{x}) \approx \mathbf{U}(\mathbf{x}=0) + \nabla\mathbf{U}|_{\mathbf{x}=0} \cdot \mathbf{x}$. The particle is located at $\mathbf{x} = 0$ and the velocity of the particle is denoted by $\mathbf{V}$, such that the relative velocity of the flow is given by $\mathbf{U}_r = \mathbf{U}(\mathbf{x}=0) - \mathbf{V}$. Such linearization can be considered appropriate provided

the flow variation over d is small but not negligible. Of course, for particle sizes greater than the scale of the ambient flow, the problem can be quite complex. The force on the particle cannot be parameterized completely in terms of $\mathbf{U}(\mathbf{x}=0)$ and $\nabla\mathbf{U}|_{\mathbf{x}=0}$ alone, and higher order gradients of $\mathbf{U}$ will be required.

In this paper, we will investigate the effect of a planar straining flow on the forces acting on a stationary spherical particle. Thus our work complements the investigation of Magnaudet *et al.* (1995), who considered the effect of axisymmetric strain. Axisymmetric strain is appropriate for particles in nozzles, in pipe flows with sudden expansion or contraction and in axisymmetric jets. On the other hand, planar strain will be appropriate in the case of planar nozzles, in sudden planar expansion or contraction and in planar jets. The effect of such large-scale mean flow gradient is also relevant for the motion of airships and underwater vessels. Apart from the mean flow effect, local turbulent velocity gradient can also play a role in determining the particle forces. There is ample experimental and computational evidence to suggest that particles tend to accumulate in regions of high strain and avoid regions of high vorticity (Wang & Maxey, 1993; Elghobashi & Truesdell 1992; Squires & Eaton, 1991). Furthermore, studies on turbulent structure (isotropic turbulence: Ashurst *et al.* (1987), convective turbulence: Balachandar (1992)) indicate that regions of local strain are more likely to be planar than axisymmetric. Thus there is sufficient interest in the investigation of particles subjected to planar strain.

The uniform relative motion, $\mathbf{U}_r$, of the undisturbed ambient flow is characterized in terms of the particle Reynolds number, Re. With the inclusion of a superimposed straining flow additional parameters are required. The strength of the straining motion is measured in terms of the variation in $\mathbf{U}$ over a particle diameter compared to $\mathbf{U}_r$. The nature of the straining flow can be varied systematically from planar strain to axisymmetric strain. The orientation of the principal axes of the strain-rate tensor relative to the direction of $\mathbf{U}_r$ can also be varied. The present investigation covers a Reynolds number range of 10 to 300, thus extending from a steady unseparated flow to periodic shedding of wake vortices, under strain-free case. Consistent with the findings of Magnaudet *et al.* (1995), even a modest planar strain has a strong influence on the flow structure around the particle. Elongational strain aligned with the direction of $\mathbf{U}_r$ tends to suppress the wake, and at sufficient strain magnitude the recirculation region is completely eliminated. On the other hand, compressional alignment of strain results in severe instability. The presence or absence of a recirculation region in the wake is likely to have a strong influence on the behavior of the drag and lift forces. When the wake region is completely suppressed, these forces follow the same pattern found in potential flow. However, with the presence of the wake, its influence can be quite complex. In this regard the structure of the wake is quite important in understanding the forces acting on the particle.

This paper will focus on the effect of planar strain on the structure of the wake. One important difference between axisymmetric and planar strain is that under planar strain the flow is three-dimensional even in the absence of unsteadiness in the wake. Azimuthal variation in the flow and correspondingly an azimuthal component of the flow exist at all Re. Of course, as Re increases the flow becomes unsteady with vortex shedding, resulting in a time-dependent three-dimensional flow, even in the absence of imposed strain. In order to properly resolve the flow details and accurately predict the lift and drag forces it is important to have a high-resolution three-dimensional and time-dependent numerical methodology. Here we employ a Fourier-Chebyshev pseudo-spectral (collocation) method which is described in section 3. The effect of strain on the structure of the wake and the surface distribution of pressure and shear stress will be considered in section 4. In this section we will also study the resulting lift and drag forces and compare them with the potential flow prediction. Discussion and conclusion will be presented in section 5.

2. Scaling Analysis

Before we embark upon the details of the wake structure and its influence on the drag and lift, we would like to establish conditions under which gradients in the ambient flow can be considered important. Based on the generalization to the BBO equation given by Maxey & Riley (1983) and on the inviscid analysis of Auton *et al.* (1988), the force on a particle subjected to an unsteady and linearly varying ambient flow at finite Re can be represented as

$$\begin{aligned}\mathbf{F} &= \mathbf{F}_{\text{std}} + m_f\frac{D\mathbf{U}}{Dt} + m_f C_M\left(\frac{\partial \mathbf{U}}{\partial t} - \frac{d\mathbf{V}}{dt}\right) + m_f C_M \mathbf{U}\cdot\nabla\mathbf{U} + m_f C_{IL}(\mathbf{U}-\mathbf{V})\times\boldsymbol{\omega} \\ &+ 3d\pi\mu\int_{-\infty}^{t} K(t-\tau,\tau)\frac{d(\mathbf{U}-\mathbf{V})}{d\tau}d\tau\,, \qquad (2.1)\end{aligned}$$

where $\mathbf{U}$ and its spatial and temporal derivatives are evaluated at the particle position. Here m_f is the mass of the fluid displaced by the particle and D/Dt and d/dt are the total derivatives following the fluid element and the particle, respectively. The first term on the right is the Stokes-like standard drag force, that would be present even in the absence of any unsteadiness or spatial variation in the undisturbed flow. The second term is the pressure gradient force due to the local temporal and convective acceleration of the ambient flow, that would also exist in the absence of the particle. The third term accounts for the added-mass effect arising from the temporal acceleration of the particle and the undisturbed flow. Here C_M is the added-mass coefficient. The fourth term is the added-mass force arising from the convective acceleration. The fifth term accounts for the lift force induced by the vorticity, $\boldsymbol{\omega} = \nabla\times\mathbf{U}$, of the undisturbed flow evaluated at the particle position, where C_{IL} is the corresponding lift coefficient. The last term is the Basset history force, which accounts for the viscous effect of unsteadiness.

From the above equation it can be seen that the convective acceleration, $\mathbf{U}\cdot\nabla\mathbf{U}$, arising from the spatial gradient plays an analogous role to the temporal acceleration, $\partial\mathbf{U}/\partial t$, in both the pressure gradient and the added-mass terms. In addition, the effect of the vortical component of the ambient flow gradient contributes to a lift force. The influence of spatial non-uniformity, if any, on the Basset history effect is not clear. The precise form of the kernel K is not fully settled even in the case of a uniform flow at finite Re (Mei & Adrian, 1992; Lovelenti & Brady 1993; Kim, Elghobashi & Sirignano, 1998).

In most studies of particle motion, the pressure gradient, added-mass and Basset history effects arising from unsteadiness in either the particle motion or the surrounding flow are normally neglected under the assumption that the particle density, ρ_{p}, is much higher than the fluid density, ρ_{f}. For lack of additional information, the pressure gradient and added-mass effects arising from the spatial non-uniformity are also ignored. Hence the particle motion is considered to be dictated mainly by the standard drag term. However, it is not clear that such simplifications are always valid. In particular, it is of interest to know if all these terms can be neglected even in the limit of heavy particles, i.e. , $\rho_{\text{f}}/\rho_{\text{p}} \ll 1$.

In the following we will use simple scaling arguments to asses the relative importance of different terms in (2.1). The analysis will be general and consider a freely moving particle, droplet or bubble in an arbitrary ambient flow. The velocity and length scales of the ambient flow are denoted by U_0 and L. For simplicity we assume that the ambient flow has no independent time scale; so the time scale is simply given by L/U_0. Further, we restrict attention to long time after the start of the motion (longer than the particle time constant) when transients arising from the particle's initial condition can be considered to have decayed. It is then reasonable to take the particle velocity $\mathbf{V}$ and the relative velocity $\mathbf{U}_r$ both scale as U_0. In such case, the density ratio $\rho_{\text{f}}/\rho_{\text{p}}$, relative size of the particle d/L and the particle Reynolds number Re are the only parameters which determine the relative strength of the various terms in (2.1).

The appropriate scaling for the fluid and particle accelerations should be established first. While

the acceleration of the undisturbed flow, $D\mathbf{U}/Dt$, simply scales as U_0^2/L, scaling of the particle acceleration, $d\mathbf{V}/dt$, is more complicated and expected to depend on ρ_f/ρ_p. In the case of particles and droplets of density ratio of order unity or less, ($\rho_f/\rho_p \leqslant 1$), the magnitude of the particle acceleration can be estimated by a leading order balance between $m_p\, d\mathbf{V}/dt$ and the standard drag force $\mathbf{F}_{std} = 3\pi\mu d f(\mathbf{U}-\mathbf{V})$. Here m_p is the mass of the particle and f is the finite Re correction to the Stokes drag. In the case of bubbles, ($\rho_f/\rho_p \gg 1$), the leading order balance is between the added-mass term $\frac{1}{2}m_f\, d\mathbf{V}/dt$ and the standard drag. The resulting appropriate scale for $d\mathbf{V}/dt$ is then

$$\frac{\rho_f}{\rho_p}\frac{f}{Re}\frac{U_0^2}{d} \qquad \text{for particles and drops } (\rho_f/\rho_p \leqslant 1)\,,$$

$$\text{and} \quad \frac{f}{Re}\frac{U_0^2}{d} \qquad \text{for bubbles } (\rho_f/\rho_p \gg 1)\,.$$

In the estimation of the Basset history term, for simplicity, the kernel is assumed to take the standard $t^{-1/2}$ decay, and the appropriate time-scale for the integral is d^2/ν for $Re \ll 1$ and d/U_0 for $Re \geqslant 1$.

The order of magnitude of different terms in (2.1) compared to the standard drag term is listed in table 1. Six different cases can be identified: for very small Reynolds number ($Re \ll 1$), the density ratio is the only deciding parameter, whereas for $Re \geqslant O(1)$, both ρ_f/ρ_p and d/L are important. Note that the contributions from $D\mathbf{U}/Dt$ and $d\mathbf{V}/dt$ can scale differently and therefore they are listed separately. The pressure gradient force and the rotational lift term scale similar to the added-mass force and therefore they are not shown in the table.

Contribution from $d\mathbf{V}/dt$ follows the expected trend: its contribution to both the added-mass and history forces is small for heavy particles, ($\rho_f/\rho_p \ll 1$), whereas it is significant in case of lighter particles and bubbles, ($\rho_f/\rho_p \approx 1$, or, $\gg 1$). This behavior is independent of the relative size of the particle or the particle Reynolds number. On the other hand, contribution from $D\mathbf{U}/Dt$ is insignificant under most conditions, except when the length-scale of the ambient flow is comparable to the particle diameter (i.e. $d/L \sim O(1)$) and when the particle Reynolds number is of $O(1)$ or higher. In which case, irrespective of the density ratio, the added-mass and history contributions from $D\mathbf{U}/Dt$ cannot be ignored.

In summary, the standard practice of neglecting the added-mass and history forces in case of heavy particles is valid provided particles are small compared to the flow scales or when the particle Reynolds number is small. However, when $d/L \sim O(1)$ and $Re \geqslant 1$, these forces have substantial effect.

3. Numerical Methodology

3.1. *Governing Equations*

We consider a spherical particle held fixed ($\mathbf{V} = 0$) at the origin $\mathbf{x} = \mathbf{0}$ of an inertial frame. Particle moving at a constant speed can be considered easily, by choosing a reference frame moving along with it and the ambient flow corrected for the particle velocity. The undisturbed flow $\mathbf{U}$ is steady, linearly varying in space and directed along the x-axis at the particle position, such that

$$\mathbf{U}(\mathbf{x}) = |\mathbf{U}_r|\,\mathbf{e}_x + (\mathbf{S}+\boldsymbol{\Omega})\,\mathbf{x}, \tag{3.1}$$

where $\mathbf{S}$ and $\boldsymbol{\Omega}$ are the pure strain and rotational part of the velocity gradient. A perturbation field $\mathbf{u}'(\mathbf{x},t)$ takes into account the deviations from the ambient flow due to the presence of the sphere. Hence the net flow field $\mathbf{u}(\mathbf{x},t)$ can be written as $\mathbf{u}(\mathbf{x},t) = \mathbf{U}(\mathbf{x}) + \mathbf{u}'(\mathbf{x},t)$. At large distances from the particle, ($\mathbf{x} \to \infty$), $\mathbf{u}(\mathbf{x},t)$ approaches the undisturbed ambient flow, and on the particle surface it satisfies no-slip and no-penetration conditions.

Re	d/L	ρ_f/ρ_p	Standard drag	Added-mass force		History force	
				$D\mathbf{U}/Dt$	$d\mathbf{V}/dt$	$d\mathbf{U}/dt$	$d\mathbf{V}/dt$
$\ll 1$		$\ll 1$	$O(1)$	$\frac{Re}{f}\frac{d}{L} : \ll 1$	$\frac{\rho_f}{\rho_p} : \ll 1$	$\frac{Re}{f}\frac{d}{L} : \ll 1$	$\frac{\rho_f}{\rho_p} : \ll 1$
		$O(1), \gg 1$			$O(1)$		$O(1)$
$O(1)$	$\ll 1$	$\ll 1$	$O(1)$	$\frac{d}{L} : \ll 1$	$\frac{\rho_f}{\rho_p} : \ll 1$	$\frac{d}{L}\frac{1}{\sqrt{Re}} : \ll 1$	$\frac{\rho_f}{\rho_p}\sqrt{Re} : \ll 1$
		$O(1), \gg 1$			$O(1)$		$O(1)$
	$O(1)$	$\ll 1$	$O(1)$	$\frac{d}{L} : O(1)$	$\frac{\rho_f}{\rho_p} : \ll 1$	$\frac{d}{L}\frac{1}{\sqrt{Re}} : O(1)$	$\frac{\rho_f}{\rho_p}\sqrt{Re} : \ll 1$
		$O(1), \gg 1$			$O(1)$		$O(1)$

TABLE 1. Order of magnitude of different terms in (2.1).

The sphere diameter d, the magnitude of the relative velocity $|\mathbf{U}_r|$ and the fluid density ρ_f are used to nondimensionalize the variables. In the following discussion any dimensionless variable will be denoted by the symbol $\tilde{}$. The governing equations for the total velocity, $\tilde{\mathbf{u}}(\tilde{\mathbf{x}}, \tilde{t})$ are given by the Navier-Stokes equations as

$$\tilde{\nabla} \cdot \tilde{\mathbf{u}} = 0\,, \tag{3.2}$$

$$\frac{\partial \tilde{\mathbf{u}}}{\partial \tilde{t}} + \tilde{\mathbf{u}} \cdot \tilde{\nabla}\tilde{\mathbf{u}} = -\tilde{\nabla}\tilde{p} + \frac{1}{Re}\tilde{\nabla}^2\tilde{\mathbf{u}}. \tag{3.3}$$

In terms of $\tilde{\mathbf{u}}'$ the above equations are

$$\tilde{\nabla} \cdot \tilde{\mathbf{u}}' = 0, \tag{3.4}$$

$$\frac{\partial \tilde{\mathbf{u}}'}{\partial \tilde{t}} + \tilde{\mathbf{u}}' \cdot \tilde{\nabla}\tilde{\mathbf{u}}' + \tilde{\mathbf{u}}' \cdot \tilde{\nabla}\tilde{\mathbf{U}} + \tilde{\mathbf{U}} \cdot \tilde{\nabla}\tilde{\mathbf{u}}' = -\tilde{\nabla}\tilde{p}' + \frac{1}{Re}\tilde{\nabla}^2\tilde{\mathbf{u}}'. \tag{3.5}$$

Here $\tilde{p}(\tilde{\mathbf{x}}, \tilde{t}) = \tilde{P}(\tilde{\mathbf{x}}) + \tilde{p}'(\tilde{\mathbf{x}}, \tilde{t})$, and $\tilde{P}(\tilde{\mathbf{x}})$ is related to $\tilde{\mathbf{U}}$ by

$$\tilde{\nabla}\tilde{P} = -\tilde{\mathbf{U}} \cdot \tilde{\nabla}\tilde{\mathbf{U}}\,. \tag{3.6}$$

The perturbation velocity $\tilde{\mathbf{u}}'$ and pressure $\tilde{p}'$ are determined by solving (3.4 - 3.5) with appropriate boundary conditions. The total flow field is then obtained by adding $\tilde{\mathbf{U}}$ and $\tilde{P}$ to them. The resultant force (in dimensional form) on the sphere is obtained by integrating the normal and the tangential stresses on the surface :

$$F_i = \int_S [-p\,\mathbf{e}_r + \tau_{r\theta}\,\mathbf{e}_\theta + \tau_{r\phi}\,\mathbf{e}_\phi] \cdot \mathbf{e}_i \,\mathrm{d}S\,. \tag{3.7}$$

The first term on the right hand side is the pressure force, while the next two terms are the viscous force. The non-dimensional force coefficient is defined as

$$\mathbf{C_F} = \frac{\mathbf{F}}{\frac{1}{2}\,\rho_f\,|\mathbf{U}_r|^2\,\pi(d/2)^2}\,. \tag{3.8}$$

The component of $\mathbf{C_F}$ along the x-axis is the drag coefficient C_D.

3.2. *Spatial Discretization*

We consider a spherical coordinate (r, θ, ϕ) (figure 1a) where

$$d/2 \leqslant r \leqslant R\,, \qquad 0 \leqslant \theta \leqslant \pi \quad \text{and} \quad 0 \leqslant \phi \leqslant 2\pi\,.$$

Here R represents the boundary of the computational domain. A Chebyshev expansion is implemented in the radial direction. The Gauss-Lobatto collocation points in r are first evaluated on $[-1, 1]$ as

$$\xi_i = -\cos\left[\frac{\pi(i-1)}{N_r - 1}\right], \tag{3.9}$$

for $i = 1, 2, ..., N_r$, where N_r is the number of radial grid points. Then a grid stretching is used to cluster points in the shear layer near the surface of the sphere. The function used for radial stretching is given by

$$\hat{\xi} = C_0 + C_1\xi - C_0\xi^2 + C_3\xi^3\,, \tag{3.10}$$

$$C_1 = .5(-\gamma_1 + 2C_0 + 3)\,, \qquad C_3 = .5(\gamma_1 - 2C_0 - 1)\,. \tag{3.11}$$

The parameters C_0 and γ_1 are used to vary the amount of stretching. The computational points in physical space are obtained using the mapping

$$r_i = \frac{1}{2}\hat{\xi}_i\left(\frac{d}{2} - R\right) + \frac{1}{2}\left(\frac{d}{2} + R\right). \tag{3.12}$$

The azimuthal direction ϕ is periodic over 2π and a Fourier expansion is used along this direction. The collocation points in ϕ are computed as

$$\phi_k = 2\pi(k-1)/N_\phi \tag{3.13}$$

for $k = 1, 2, ..., N_\phi$, where N_ϕ is the number of grid points in ϕ. In the tangential direction θ, it is sufficient to define the variables over the interval $0 \leqslant \theta \leqslant \pi$; however, the variables are periodic over 2π, and not over π. Thus a Fourier collocation in θ can be used only with some symmetry restrictions. One may note that a scalar, the radial component of a vector, and the radial derivative of a scalar are continuous over the poles ($\theta = 0$ and π). But the tangential and the azimuthal components of a vector change sign across the poles. The tangential and azimuthal derivatives of a scalar also change sign. It is the so-called 'parity' problem in spherical geometry, and has been discussed by Merilees (1973), Orszag (1974) and Yee (1981). The problem of pole-parity does not arise if surface harmonics are used. However, spectral methods using surface harmonics require $O(N)$ operations per mode, while those based on Fourier series require only $O(\log N)$ operations. In the present study, a suitable Fourier expansion in θ is derived formally by following Shariff's (1993) approach. We start by considering a typical term in the expansion:

$$\begin{Bmatrix} \tilde{c} \\ \tilde{u}_r \\ \tilde{u}_\theta \end{Bmatrix} = \begin{Bmatrix} \alpha \\ \beta \\ \gamma \end{Bmatrix} \tilde{r}^p \exp(im\theta)\exp(ik\phi) \tag{3.14}$$

where $\tilde{c}$ represents a scalar. The method requires that a scalar and the Cartesian components of a vector each independently be analytic at the poles. Such a requirement results in the following acceptable expansions:

$$\tilde{c} = \begin{Bmatrix} \sum \alpha_{pmk} T_p(\tilde{r})\cos(m\theta)\exp(ik\phi) & \text{even} \quad k \\ \sum \alpha_{pmk} T_p(\tilde{r})\sin(m\theta)\exp(ik\phi) & \text{odd} \quad k \end{Bmatrix}, \tag{3.15}$$

$$\tilde{u}_r = \left\{ \begin{array}{ll} \sum \beta_{pmk} T_p(\tilde{r}) \cos(m\theta) \exp(ik\phi) & \text{even } k \\ \sum \beta_{pmk} T_p(\tilde{r}) \sin(m\theta) \exp(ik\phi) & \text{odd } k \end{array} \right\} \tag{3.16}$$

and

$$\tilde{u}_\theta = \left\{ \begin{array}{ll} \sum \gamma_{pmk} T_p(\tilde{r}) \sin(m\theta) \exp(ik\phi) & \text{even } k \\ \sum \gamma_{pmk} T_p(\tilde{r}) \cos(m\theta) \exp(ik\phi) & \text{odd } k \end{array} \right\}, \tag{3.17}$$

where T_p represents p^{th} Chebyshev polynomial and $i = \sqrt{-1}$. m and k are the wave-numbers in θ and ϕ directions. α, β and γ are the coefficients in the expansions and are functions of p, m and k. The expansion for $\tilde{u}_\phi$ follows that of $\tilde{u}_\theta$.

The collocation points in θ are distributed as

$$\hat{\theta}_j = \frac{\pi}{N_\theta} [j - 1/2] , \tag{3.18}$$

for $j = 1, 2, ..., N_\theta$, where N_θ is the number of grid points in θ. A grid stretching is used to cluster points in the wake region of the sphere as

$$\theta_j = \tan^{-1} \left[\frac{\sin(\hat{\theta}_j)(1 - \hbar^2)}{\cos\hat{\theta}_j (1 + \hbar^2) - 2\hbar} \right] , \tag{3.19}$$

where $\hbar$ is the parameter that controls the degree of stretching. In the simulations to be reported here, a value of $\hbar = -0.35$ provides sufficient resolution in the sphere wake. A ϕ-projection of a typical mesh is shown in figure 1b.

3.3. *Temporal Discretization*

A two-step time-split method is used to advance $\tilde{\mathbf{u}}'$ in time. In the first step the velocity field is advanced from time level 'n' to an intermediate level '*' by solving the advection diffusion equation

$$\frac{\tilde{\mathbf{u}}'_\star - \tilde{\mathbf{u}}'_n}{\Delta\tilde{t}} + \mathbf{NL}(\tilde{\mathbf{u}}'_n) = \frac{1}{Re}\mathbf{D}(\tilde{\mathbf{u}}'_\star) , \tag{3.20}$$

where $\mathbf{D}$ and $\mathbf{NL}$ are the diffusion and nonlinear terms. This is followed by a pressure correction step

$$\frac{\tilde{\mathbf{u}}'_{n+1} - \tilde{\mathbf{u}}'_\star}{\Delta\tilde{t}} = -\tilde{\nabla}\tilde{p}'_{n+1} . \tag{3.21}$$

By satisfying the divergence free condition, $\tilde{\nabla} \cdot \tilde{\mathbf{u}}'_{n+1} = 0$, a Poisson equation for pressure is obtained from (3.21) as

$$\tilde{\nabla}^2 \tilde{p}'_{n+1} = \frac{\tilde{\nabla} \cdot \tilde{\mathbf{u}}'_\star}{\Delta\tilde{t}} . \tag{3.22}$$

The above equation is solved fully implicitly for $\tilde{p}'_{n+1}$ and the intermediate velocity $\tilde{\mathbf{u}}'_\star$ is then corrected by (3.21) to obtain $\tilde{\mathbf{u}}'$ at $(n+1)$. In the advection-diffusion step, the non-linear and the cross-derivative terms are treated explicitly using second order Adams-Bashforth scheme. The θ-diffusion term is also treated explicitly. To avoid severe viscous stability constraint due to the grid stretching near the surface, the radial diffusion term is treated implicitly using a Crank-Nicholson scheme. The azimuthal diffusion term decouples from the rest of the operators when the momentum equation is transformed to Fourier space; hence it is also treated implicitly.

3.4. *Boundary Conditions*

Spectral methods are extremely sensitive to boundary conditions due to their global nature. Only carefully derived boundary conditions will produce stable and consistent results. At the inflow, the Dirichlet boundary condition specifying the undisturbed ambient flow is used. At the outflow, a

non-reflecting boundary condition by Mittal & Balachandar (1996) is used. The idea is to smoothly parabolize the governing equations by multiplying the radial diffusion terms by a filter function. The filter function is such that the diffusion terms are unaltered in most of the computational domain, while at the outflow boundary they smoothly vanish. Hence the method does not require any explicit outflow boundary condition and the governing equations are solved there.

On the surface of the sphere, no-slip and no-penetration conditions are imposed for the total velocity field $\tilde{\mathbf{u}}$. This is equivalent to the condition that $\tilde{\mathbf{u}}' = -\tilde{\mathbf{U}}$ on the sphere surface. In the context of time split scheme the appropriate boundary condition for the intermediate velocity is

$$\tilde{\mathbf{u}}'_\star = -\tilde{\mathbf{U}} + \Delta\tilde{t}(2\tilde{\nabla}\tilde{p}'_n - \tilde{\nabla}\tilde{p}'_{n-1})\,. \tag{3.23}$$

Combined with the homogeneous Neumann boundary condition for pressure, $\partial\tilde{p}'_{n+1}/\partial\tilde{r} = 0$, (3.23) guarantees zero penetration through the surface of the sphere, while the no-slip condition is satisfied to order $O(\Delta\tilde{t}^3)$. A typical $\Delta\tilde{t}$ used in the present study is 0.001.

3.5. *Pole Stability*

Due to the topology of the grid, the azimuthal resolution is spatially nonuniform. The resolution is much higher near the poles compared to the equator. Furthermore, the azimuthal grid spacing linearly decreases with the radial location as the surface of the sphere is approached. The viscous stability constraint due to such nonuniform resolution is avoided by the implicit treatment of the radial and the azimuthal diffusion terms. However, the time-step size is still restricted by the convective stability (CFL) condition. Ideally it is desirable to have higher spatial resolution only in regions as demanded by the local flow structure. A simple strategy to remove higher ϕ resolution in regions where it is not needed is to filter high frequency components. Such a filter necessarily has to be a function of both $\tilde{r}$ and θ.

There are some constraints that must be satisfied by the pole filter. It must be sufficiently smooth in all its variables to preserve spectral convergence. The analytic nature of the scalar and vector fields requires that in the limit $\theta \to 0$ and π, only the azimuthal modes $k = 0$ and $k = \pm 1$ exist in the expansions (3.15) - (3.17). Physically, $k = 0$ is the axisymmetric mode and it does not contribute to the pole stability constraint. The $k = \pm 1$ modes are the most unstable and lead to bifurcation in the flow (Natarajan & Acrivos, 1993). Hence, to the lowest order, these modes must be retained over the entire computational domain. From CFL criterion, it can be inferred that as long as the ϕ spectra of the velocity field decays faster than $(k)^{-2}$, the time-step is dictated by the $k = \pm 1$ mode. Based on this observation, we introduce a pole filter function given by

$$f_\phi = 1 - \exp\left[-\lambda_1 Y^{\lambda_2}\right]\,, \tag{3.24}$$

where $Y = \tilde{r}\,\sin\theta$. λ_1 and λ_2 are functions of k and are determined by the conditions

$$f_\phi = \frac{1}{k} \quad \text{at} \quad Y = Y_{\min} \qquad \text{and} \qquad f_\phi = 0.9 \quad \text{at} \quad Y = kY_{\min}\,. \tag{3.25}$$

Here $Y_{\min}$ is the value of Y at the grid-point closest to the pole on the sphere (note that in (3.18) the θ discretization has been chosen to avoid $\theta = 0$ and π points). Thus the filter function attempts to achieve at least $(k)^{-2}$ decay at the point closest to the pole. However, the filter function approaches unity exponentially such that at a distance $kY_{\min}$ form the pole, f_ϕ approaches 0.9. Thus filtering is localized to a very small region near the poles close to the sphere. The size of the filtered region slowly increases with the azimuthal mode number. The filter is applied on the intermediate velocity field $\tilde{\mathbf{u}}'_\star$ at the end of the advection-diffusion step.

4. Results and Discussion

4.1. *Uniform Flow*

Before presenting the results for planar straining flow we will first consider the case of uniform flow. Simulations are performed in the range $10 \leqslant Re \leqslant 500$ to cover four different flow regimes: unseparated flow for $Re < 20$, steady axisymmetric flow with separation for $20 < Re < 210$, steady non-axisymmetric flow for $210 < Re < 270$ and unsteady vortex shedding for $Re > 270$.

Streamline pattern for $Re = 10$ is shown in figure 2a. Here the flow direction is from left to right. Flow does not separate at this Re, but there is asymmetry about $\theta = \pi/2$ in the vicinity of the sphere which indicates departure from Stokes flow. The onset of separation occurs at around $Re = 20$ (Le Clair *et al.*, 1970; Dennis & Walker, 1971). Corresponding streamlines at $Re = 100$ are shown in figure 2b. The steady separated flow appears as an axisymmetric toroidal eddy behind the sphere. The topological structure of the wake remains the same up to $Re = 210$.

At around $Re = 210$, axisymmetric nature of the wake is broken by a regular bifurcation (Natarajan & Acrivos, 1993; Tomboulides *et al.*, 1993). Unlike a two dimensional bluff body, symmetry-breaking in the sphere wake does not initiate vortex shedding process and the wake remains steady for approximately $210 < Re < 270$. In this regime, the wake consists of two streamwise vortices which are opposite in sign and appear as two distinct dye threads emanating from the end of the recirculating region. It is commonly known as the "double threaded" wake and has a plane of symmetry (the $x-y$ plane, in the present case). Figure 2c (view along the $x-y$ plane) and 2d (view normal to the $x-y$ plane) show the double threaded structure for $Re = 250$. Here the vortical structure is extracted in terms of an iso-surface of the imaginary part of the complex conjugate eigenvalue of the velocity gradient tensor (see Zhou, Adrian, Balachandar & Kendall, 1999 for details). Above $Re = 270$, the steady non-axisymmetric wake undergoes Hopf bifurcation resulting in periodic shedding of vortices. The hairpin-shaped vortical structures are shown in figure 2e and 2f for $Re = 350$. Even at this Re, a plane of symmetry (the $x-y$ plane) in the wake is present which remains fixed in time. As a result, in contrast to a two dimensional body where vortices are shed alternately from two sides, here vortices are shed in the same orientation. The vortical structure consists of a chain of interlocking loops which is similar to the structure postulated by Achenbach (1974). The results presented here agree well with the simulations of Mittal (1999), Johnson & Patel (1999), Tomboulides *et al.* (1993), and flow visualizations by Sakamoto & Haniu (1990) and Magarvey & Bishop (1961).

A quantitative comparison with previous results is shown in table 2. The drag coefficient C_D, obtained from present simulations agree well with the experimental correlation of Clift *et al.* (1978). Good agreement is also observed with the numerical results obtained by Mittal (1999) and Magnaudet *et al.* (1995). The separation angle, θ_s, measured from the rear stagnation point and the length of the recirculation eddy, L_e, measured from the base of the sphere and normalized by the sphere diameter are also presented for the steady regime. Here also good agreement is found with the data given in Clift *et al.* (1978) and the simulation results of Magnaudet *et al.* (1995). The separation angle and recirculation length are not reported for the non-axisymmetric and unsteady cases, as in these regimes the recirculation eddy is not a closed bubble and the separation line on the sphere surface is no longer axisymmetric. Non-axisymmetry in the wake, however, produces a lift force and the corresponding lift coefficient, C_L, at $Re = 250$ is found to be the same as that reported in Johnson & Patel (1999). Further comparison in the unsteady regime can be made for the dimensionless shedding frequency or the Strouhal number, St. At $Re = 350$, St reported by Sakamoto & Haniu (1995) lies between $0.13 - 0.14$ while Mittal's (1999) simulation predicts $St = 0.138$. These results are in reasonable agreement with the present value of 0.135. Similar agreement is found at $Re = 500$, where the present simulation predicts $St = 0.175$ against the experimental range of $0.17 - 0.18$.

The adequacy of grid resolution can be investigated in terms of the decay of the energy spectra

Re	Present simulations					Previous results				
	C_D	C_L	θ_s	L_e/d	St	C_D	C_L	θ_s	L_e/d	St
10	4.30					4.32†				
50	1.57		40.8	0.41		1.54*, 1.57**		40.0†	0.44*	
100	1.09		53.2	0.87		1.09*, 1.09**		53.6†	0.87*	
200	0.77		63.7	1.43		0.80*, 0.765†		65.0†	1.29†	
250	0.70	−0.06				0.73*, 0.68**	−0.06‡			
350	0.62				0.135	0.64*, 0.62**				0.13 − 0.14¶
500	0.56	0.04			0.175	0.56*				0.17 − 0.18¶

TABLE 2. Comparison of present simulations with previous experimental and numerical results for uniform flow past a sphere. * Clift *et al.* (1978); ** Mittal (1999); † Magnaudet *et al.* (1995); ‡ Johnson & Patel (1999); ¶ Sakamoto & Haniu (1995).

with respect to wavenumber. Here we present the energy spectra for a uniform flow at $Re = 500$. For this simulation a grid of $N_r = 81, N_\theta = 96$ and $N_\phi = 32$ points is used. The radial resolution in terms of Chebyshev spectra, measured at two different locations in the near wake, is shown in figure 3a. At least 7 orders of magnitude decay is observed. Figure 3b shows the θ spectra at two different radial locations: within the boundary layer, and at a downstream location far from the sphere. Here also at least 7 orders of magnitude decay in energy is observed. The ϕ spectra is shown in figure 3c for which a minimum decay of 9 orders is found. The chosen grid therefore provides adequate resolution for Re up to 500. Similar checks on the adequacy of resolution have been performed for all other cases including straining flows.

Further validation of the present computational approach in linearly varying flows is given in table 3. Here we consider an axisymmetric straining flow and a linear shear flow for varying Reynolds number and dimensionless strain or shear magnitude, s (to be defined later). The drag coefficient, separation angle and the recirculation length obtained from our simulations are consistent with Magnaudet *et al.*'s (1995) results for the straining flow. For the shear flow case, the drag and lift coefficients are in good agreement with the results of Komori and Kurose (1996).

4.2. *Planar Strain*

In this section we will present the results of a stationary spherical particle subjected to a steady ambient flow consisting of a uniform flow and a planar straining flow. The results will be compared with axisymmetric straining flow considered by Magnaudet *et al.* (1995). The uniform flow is given by the relative flow velocity at $\mathbf{x} = 0$, and in non-dimensional terms $\tilde{\mathbf{U}}_r = \mathbf{e}_x$. The strain-rate tensor for planar strain is given by

$$\tilde{\mathbf{S}} = \begin{bmatrix} s\cos 2\Theta \cos^2\Phi & s\sin 2\Theta\cos\Phi & -s\cos 2\Theta\sin\Phi\cos\Phi \\ s\sin 2\Theta\cos\Phi & -s\cos 2\Theta & -s\sin 2\Theta\sin\Phi \\ -s\cos 2\Theta\sin\Phi\cos\Phi & -s\sin 2\Theta\sin\Phi & s\cos 2\Theta\sin^2\Phi \end{bmatrix}, \tag{4.1}$$

Imposed flow	Parameters	Present simulations					Previous results				
		C_D	C_L	θ_s	L_e/d	St	C_D	C_L	θ_s	L_e/d	St
Axisymmetric strain	$Re = 100$ $s = 0.1$	1.38		42.5	0.38		1.39		43	0.37	
	$Re = 100$ $s = 0.2$	1.65		33.9	0.21		1.66		35	0.20	
	$Re = 200$ $s = 0.1$	1.07		51.3	0.57		1.06		54	0.60	
	$Re = 300$ $s = 0.1$	0.92		58.6	0.77		0.92		60	0.76	
Linear shear	$Re = 200$ $s = 0.2$	0.79	−0.058				0.80	−0.05			
	$Re = 400$ $s = 0.2$	0.62	−0.075			0.19	0.62	−0.07			0.15 - 0.17

TABLE 3. Comparison of present simulations with previous numerical results for nonuniform flows over a sphere. Results for axisymmetric strain are compared with Magnaudet *et al.* (1995); results for linear shear flows are compared with Kurose & Komori (1999).

where $\tilde{\mathbf{S}} = \mathbf{S}d/|\mathbf{U}_r|$, and s is the dimensionless strain magnitude. The angles Θ and Φ measure the relative orientation of the planar strain with respect to $\tilde{\mathbf{U}}_r$. The following orientations are considered in this study :

a) Elongational strain along relative velocity: $\Theta = 0$ and $\Phi = 0$;
b) Compressional strain along relative velocity: $\Theta = \pi/2$ and $\Phi = 0$;
c) Relative velocity along the plane of strain: $\Theta \neq 0$ or $\pi/2$ and $\Phi = 0$;
d) Relative velocity away from the plane of strain: $\Theta = 0$ and $\Phi \neq 0$.

These orientations are schematically shown in figure 4. For axisymmetric strain, cases c and d are the same, whereas for planar strain they are different. In the following sections we will consider each of these cases in detail.

4.2.1 *Elongational strain along relative velocity* ($\Theta = 0, \Phi = 0$)

The influence of strain on the structure of the wake can be observed in terms of changes in the length of the recirculation eddy, separation angle and limiting streamlines on the sphere surface. The identification of separation line for a three-dimensional flow has been a subject of interest for many years. The issue is discussed by Tobak and Peake (1982). One way to identify the separation line is to draw the skin friction lines or the limiting streamlines from the two-dimensional vector field given by the shear stresses $\tau_{r\theta}$ and $\tau_{r\phi}$ on the surface of the sphere. For an axisymmetric

flow, $\tau_{r\theta}$ and $\tau_{r\phi}$ vanish simultaneously along the line of separation and the separation is defined as singular separation. For three-dimensional separation, a second type of separation exists in which the limiting streamlines merge together to form a separation line. For the latter type of separation, both $\tau_{r\theta}$ and $\tau_{r\phi}$ need not vanish simultaneously.

The surface streamlines for uniform flow at $Re = 200$ are shown in figure 5a. The view shown is the end view looking along the negative x direction. The separation line is a perfect circle due to the steady axisymmetric nature of the wake. The unsteady non-axisymmetric regime in uniform flow is considered in figure 5b for $Re = 300$. Since the flow is time-dependent, the surface streamlines in this figure correspond to an instant in the vortex shedding cycle. Here the $x - y$ plane can be identified as the plane of symmetry. Though the line of separation is nearly circular, non-axisymmetric nature of the wake is clear from the surface streamline patterns. The separation line does not change significantly over the shedding cycle; however the rear stagnation point oscillates on the $x - y$ plane. The drag and lift forces change periodically and the time-averaged lift remains non-zero. The effect of an axisymmetric elongational strain imposed on the uniform flow is to stabilize the flow and delay bifurcation to the non-axisymmetric and unsteady regimes. At $Re = 300$, in figure 5c, the axisymmetric nature of the wake is recovered under the influence of an axisymmetric strain of magnitude $s = 0.1$. Consequently, the lift force is zero and the drag force remains steady in time. Evolution of the drag coefficient over time is shown in figure 6 for the axisymmetric strain case and compared with the uniform flow result.

The effect of planar strain on the surface streamlines is shown in figure 5d for $Re = 300$ and $s = 0.1$. Due to the three-dimensional nature of planar strain it is natural to expect the separation line to be non-axisymmetric. On the other hand, the strong favorable pressure gradient associated with elongational straining flow tends to stabilize the wake and preserve axisymmetry. The surface streamlines on the sphere appear to be strikingly similar in both planar and axisymmetric strain cases. Similar to the axisymmetric case, planar strain delays bifurcation to the unsteady regime. The resulting lift force in planar strain is also zero and the drag force remains steady over time. Time evolution of the drag coefficient in planar strain is shown in figure 6.

In axisymmetric straining flow, at moderate Re, the azimuthal component of velocity u_ϕ, as well as the shear stress $\tau_{r\phi}$ are zero. Thus, at any ϕ plane, the location of separation is identified by the condition $\tau_{r\theta} = 0$. In planar strain, however, $\tau_{r\phi}$ is zero only on the $x - y$ and $x - z$ planes. Hence the condition $\tau_{r\theta} = 0$ can be used in these planes only. The difference in separation angles in the two planes will provide a quantitative information about non-axisymmetry of the wake. Separation angles measured from the rear stagnation point are listed in table 4. The results of uniform flow ($s = 0.0$) are also listed for comparison. First, we observe that the presence of an elongational strain delays the onset of separation with increasing s by imposing a favorable pressure gradient over $\theta < \pi/2$. Secondly, consistent with the nature of planar strain, separation on the $x - z$ plane occurs slightly ahead than on the $x - y$ plane. Nevertheless, the difference between the separation angles on the $x - y$ and $x - z$ planes is small, which implies that the separation line is nearly circular even in case of planar strain. The results of the planar strain cases may also be compared with the axisymmetric strain cases given in table 3. Consistent with our observation of surface streamlines, separation location in case of planar strain is very close to that for axisymmetric strain.

Further insight into the non-axisymmetric nature of the wake can be gained by considering the trajectory of a fluid element. In the regime of steady axisymmetric flow, the path lines (or streamlines) remain on individual ϕ planes and there is no mixing of fluid across these planes. Furthermore, the recirculation region is closed and the fluid inside is entrapped. In the unsteady non-axisymmetric regime, the recirculation region is not closed and there is significant mixing across different ϕ-planes. The path lines of two fluid elements emanating symmetrically from both sides of the $x - y$ plane are shown in figure 7a for uniform flow at $Re = 300$. Corresponding view along the $x - z$ plane is shown in figure 7b where the path lines coincide. The fluid element from

	Plane	$s = 0.0$	$s = 0.05$	$s = 0.1$	$s = 0.2$	$s = -0.04$
$Re = 50$	$x-y$	40.8	33.5	27.5		46.5
	$x-z$		34.2	27.2		45.5
$Re = 100$	$x-y$	53.2	46.9	41.8	34.6	58.4
	$x-z$		48.1	43.3	33.6	57.3
$Re = 200$	$x-y$	63.7	57.2	52.3	45.5	69.8
	$x-z$		58.6	53.6	45.7	69.0

TABLE 4. Effect of planar strain on separation angles. Here $x-y$ and $x-z$ are the planes where θ_s is measured.

the upstream side is drawn around the upper focus of the recirculation eddy (located on the $x-y$ plane for $y > 0$). Then it travels around the lower focus (located on the $x-y$ plane for $y < 0$) and the upper focus several times before being ejected from the eddy and joining the downstream flow. The stable or unstable nature of the upper and lower foci alternates periodically over a shedding cycle. The path-lines are separated to the left and right of the $x-y$ plane and there is no mixing across this plane. However, significant mixing occurs on each side of the plane.

Application of planar strain significantly affects mixing as shown in figure 7c and d for the case $Re = 300, s = 0.1$. We consider trajectory of two fluid elements which are initially located symmetrically on either side of the $x-y$ plane. The fluid element is first drawn towards the stable foci located on the $x-z$ plane. As it spirals inwards, it is gradually pushed out of the $x-z$ plane and towards the unstable foci located on the $x-y$ plane. The path lines in the figure indicate the direction of azimuthal velocity from one focus to the other. As the unstable foci are approached, the fluid elements begin spiraling outward and finally join the downstream flow. Note that for planar strain, both $x-y$ and $x-z$ planes are the symmetry planes. Thus fluid is confined to only one quadrant of the separation eddy resulting in less mixing. Also unlike the uniform flow case at $Re = 300$, the stable or unstable nature of the foci is fixed in time. Trajectory of the fluid elements and nature of the foci remain similar at other Reynolds numbers and strain magnitude as well.

The length of the recirculation region L_e normalized by the sphere diameter d is presented in figure 8. Here, L_e is measured from the sphere surface at $\theta = 0$ to the reattachment point. In elongational strain, the length decreases with higher strain magnitude; for example at $Re = 100, s = 0.2$, L_e/d is found to be 0.22 against its value of 0.87 in uniform flow. Given a strain of sufficient magnitude, the recirculation eddy may be suppressed completely as in the case of $Re = 50, s = 0.2$. Similar to separation angles, the length of the recirculation eddy at a given Reynolds number and strain magnitude is nearly the same in both planar and axisymmetric strain (see table 3 for axisymmetric results).

For the case of elongational planar strain, the particle experiences only a drag force. Corresponding drag coefficient, C_D, is compared with the uniform flow result in figure 9a. A significant increase in C_D under the influence of strain is observed. In terms of percentage change, increase in C_D is much larger at higher Reynolds numbers. For example, at $Re = 300$ and $s = 0.2$, C_D increases by nearly 87%; on the other hand, at $Re = 10$ and for the same value of s, the increase is about 25%. The drag coefficient can be further separated into the pressure and viscous contributions, C_{PD} and C_{VD}, which are shown in figure 9b and 9c. In the absence of imposed strain the

Strain	Re	10	50	100	200	300
Planar	C_D	4.31 (5.38)	1.59 (3.48)	1.09 (3.21)	0.78 (2.95)	.66 (2.86)
	C_{PD}	1.51 (2.96)	.662 (2.37)	.51 (2.31)	.42 (2.26)	.38 (2.24)
	C_{VD}	2.8 (2.44)	.93 (1.09)	.58 (.88)	.36 (.71)	.28 (.66)
Axisymmetric*	C_D	4.32 (4.33)		1.10 (2.81)	.77 (2.70)	.65 (2.72)
	C_{PD}	1.49 (2.57)		.51 (1.96)	.40 (2.04)	.37 (2.08)
	C_{VD}	2.83 (1.76)		.59 (.86)	.37 (.65)	.27 (.65)

TABLE 5. The y-intercepts and slopes of the best-fit linear curves for the planar and axisymmetric strain data. The values in bracket are the slopes. *, axisymmetric data are obtained from Magnaudet *et al.*'s (1995) simulations.

pressure contribution dominates for $Re > 100$. However, over the entire range of Re, the strain induced increase in the pressure drag is larger than that in the viscous drag. The difference is small at low Reynolds numbers, but increases substantially at higher Re.

Evolution of the drag coefficients with increasing strain magnitude is shown in figure 10 for $Re = 10$, 50 and 300. The variation is nearly linear with s, and similar trend is observed at other Reynolds numbers. At $Re = 10$, contribution from the viscous drag dominates over pressure drag, and both increase nearly at the same rate. At higher Re, the pressure drag increases at a faster rate than viscous drag. This effect can be clearly seen at $Re = 50$, where the viscous contribution is larger for weak strain, whereas the pressure contribution is dominant in the range $s > 0.2$. This trend continues as Re increases and at $Re = 300$ for all s, the pressure contribution dominates. From figure 10, it is clear that the drag coefficients can be expressed as the sum of two quantities: a baseline drag that corresponds to the uniform flow and a linearly increasing contribution due to strain,

$$C_D(Re, s) = A_D(Re) + B_D\, s \tag{4.2}$$

$$C_{PD}(Re, s) = A_{PD}(Re) + B_{PD}\, s \tag{4.3}$$

$$C_{VD}(Re, s) = A_{VD}(Re) + B_{VD}\, s. \tag{4.4}$$

Table 5 lists the intercept along the ordinate (A) and the slope (B) obtained from the linear fit of the data shown in figure 10. The intercept values for the total, pressure and viscous drag components are indeed very close to the corresponding values for uniform flow, i.e., $A_D(Re) \approx C_D(Re, 0)$, etc.

The above results for planar strain are qualitatively similar to axisymmetric strain considered by Magnaudet *et al.* (1995). The baseline total, pressure and viscous drag components are nearly the same in planar and axisymmetric cases. However, the slopes are different (see table 5). While the difference is small in viscous contribution, it is substantial in pressure contribution. For the planar strain cases, the values of B_{PD} and B_{VD} are somewhat higher, which implies that the drag is higher in planar strain than in axisymmetric strain.

One can use potential flow analysis as the basis for obtaining a fair comparison between the two cases. In order to do so, the dimensionless strain-rate tensor for $\Theta = 0$, $\Phi = 0$ for both axisymmetric and planar strains is written in a combined fashion as:

$$\tilde{\mathbf{S}} = \begin{bmatrix} s & 0 & 0 \\ 0 & -f_s s & 0 \\ 0 & 0 & (f_s - 1)s \end{bmatrix}. \tag{4.5}$$

The parameter f_s accounts for the nature of strain; it is bounded between 1/2 (axisymmetric strain) and 1 (planar strain). The velocity potential for an ambient flow $\tilde{\mathbf{U}} = \mathbf{e}_x + \tilde{\mathbf{S}} \cdot \mathbf{x}$ can be written as

$$\begin{aligned} &\left(\tilde{r} + \frac{1}{16\tilde{r}^2}\right)\cos\theta + s\left(\frac{\tilde{r}^2}{2} + \frac{1}{96\tilde{r}^3}\right)\left(\frac{3}{2}\cos^2\theta - \frac{1}{2}\right) \\ &+ \quad s\left(\frac{1}{2} - f_s\right)\left(\frac{\tilde{r}^2}{4} + \frac{1}{192\tilde{r}^3}\right)\sin^2\theta\cos 2\phi\,. \end{aligned} \tag{4.6}$$

The first term is due to the uniform flow, and the remaining terms represent contributions from strain. Using the Bernoulli equation, the pressure coefficient on the surface of the sphere is evaluated as

$$\begin{aligned} C_p = 1 &- \left[-\frac{3}{2}\sin\theta + \frac{5}{12}s\left(\frac{1}{2} - f_s\right)\sin 2\theta\cos 2\phi - \frac{5}{8}s\sin 2\theta\right]^2 \\ &- \left[\frac{5}{6}s\left(\frac{1}{2} - f_s\right)\sin\theta\sin 2\phi\right]^2 \end{aligned} \tag{4.7}$$

The above surface pressure distribution yields a drag coefficient of $2\,s$, which is surprisingly independent of the planar or axisymmetric nature of strain. This behavior is also implied in the inviscid analysis of Taylor (1928) and Auton *et al.* (1988). Therefore, for potential flow the only quantity that matters is the strain magnitude s, which can be interpreted as the component of $\tilde{\mathbf{S}}$ along relative velocity. Exact partitioning of the strain-rate tensor along the other two directions does not matter. A comparison of the numerical results for the planar and axisymmetric strain cases presented in table 5 shows that this indifference to the nature of strain for potential flow may not be entirely accurate at finite Reynolds numbers. For the same s, planar strain results in larger drag. One possible explanation could be that the overall strain magnitude, measured in terms of $\sqrt{\mathrm{tr}(\tilde{\mathbf{S}}^2)}$ is larger for planar strain than for axisymmetric strain.

The influence of strain on the pressure drag can be illustrated further by looking at the distribution of the pressure coefficient, C_P, on the surface of the sphere. For the uniform flow and axisymmetric strain cases, pressure distribution is independent of the azimuthal angle, ϕ. For the case of planar strain, pressure is non-axisymmetric and hence C_P at selected ϕ-planes will be considered. For the latter case, it is also convenient to use a ϕ-averaged pressure coefficient defined as

$$\langle C_P \rangle = \frac{1}{2\pi}\int_0^{2\pi} C_P\, d\phi\,. \tag{4.8}$$

First, we will consider the surface pressure distribution in potential flow. Six different curves are shown in figure 11a that correspond to a uniform flow case and planar and axisymmetric strain cases, both at $s = 0.2$. For the planar strain case, C_P at three different ϕ-planes, $\phi = 0, \pi/4$ and $\pi/2$, and $\langle C_P \rangle$ are plotted. The front stagnation pressure is used as reference. Pressure distribution is symmetric about $\theta = \pi/2$ in the uniform flow case resulting in zero drag. The effect of strain is to introduce a fore-aft asymmetry about $\theta = \pi/2$ which produces a finite drag. The decrease in favorable pressure on the upstream side is somewhat slowed down, but the region of favorable pressure gradient extends into the leeward side. In the case of planar strain, the effect is the largest along $\phi = 0$ and the smallest along $\phi = \pi/2$. Difference between $\langle C_P \rangle$ for planar and axisymmetric strains is of $O(s^2)$ and is indistinguishable in the figure.

Surface pressure distribution for $Re = 100$ is shown in figure 11b. Five different curves are plotted: C_P for uniform flow, and for axisymmetric strain at $s = 0.2$; C_P along $\phi = 0$ and $\pi/2$ and $\langle C_P \rangle$ for planar strain at $s = 0.2$. On the windward side, similar to potential flow, the effect of strain is to slow down and prolong the favorable pressure gradient. On this side, difference bewteen the two strain cases is small. However, significant difference exists in the leeward side. The wake pressure is lower in planar strain than in axisymmetric strain which results in a higher pressure drag for the former case.

Unlike the pressure drag, the viscous drag has no analog in potential flow. We will consider variation of surface vorticity to study the effect of strain on the viscous drag. In a three-dimensional flow field, there are two orthogonal components of surface vorticity: the tangential component, ω_θ, and the azimuthal component, ω_ϕ. Under steady flow conditions, $\omega_\theta = 0$ in case of axisymmetric strain, whereas, in planar strain, the ϕ-averaged tangential vorticity $\langle \omega_\theta \rangle$ is zero. Hence ϕ-averaged azimuthal vorticity $\langle \omega_\phi \rangle$ alone can be used to illustrate the effect of planar strain on vorticity, and on the viscous drag. The distribution of $\langle \omega_\phi \rangle$ is shown in figure 12a for $Re = 10$. Three different cases are considered: uniform flow, axisymmetric strain at $s = 0.1$ and planar strain at $s = 0.1$. Corresponding results for $Re = 300$ are shown in figure 12b. There are two different mechanisms that influence the distribution of surface vorticity under a straining flow. First, in addition to the uniform flow, the imposed strain field must also satisfy the no-slip condition. As a result, for an elongational strain, the surface vorticity from the strain component is opposite to that arising from the uniform flow on the upstream side ($\theta > \pi/2$); on the downstream side ($\theta < \pi/2$), ahead of flow separation the two contributions are of the same sign. Although the effect of strain is to shrink the separated region, the strength of the recirculation eddy is enhanced as indicated by the increased magnitude of surface vorticity in the wake. This corresponds well with the enhanced the viscous drag in the presence of elongational strain. The second mechanism leading to change in vorticity distribution is the strain-induced vortex stretching mechanism. This mechanism also causes the magnitude of the surface vorticity to increase for $\theta < \pi/2$ and decrease for $\theta > \pi/2$. Thus the overall effect of strain is to increase viscous drag. As observed in table 5, the effect is strong in planar strain at low Re. With increasing Re, the effect is nearly independent of the nature of strain.

4.2.2 *Compressional strain along relative velocity* ($\Theta = \pi/2, \Phi = 0$)

In this section we present the results of a compressional planar strain ($s < 0$) imposed on a uniform flow; in other words we consider the case $\Theta = \pi/2$, $\Phi = 0$ as shown in figure 4b. Magnaudet *et al.* (1995) have studied the same configuration for axisymmetric strain. It is observed that the vorticity generated on the surface of the sphere is intensified as it convects along the streamwise direction. The undisturbed flow, $\mathbf{U}$, has a stagnation plane downstream of the sphere at $x = -2/s$ (for elongational strain, $s > 0$, this plane is located upstream of the sphere). For the compressional planar strain case, the stagnation plane is located at $x = -1/s$. A vortical wake from the sphere approaches this stagnation plane from upstream and the irrotational ambient flow approaches the stagnation plane from downstream. Thus there is a discontinuity in vorticity at $x = -1/s$. At a low Reynolds number, such discontinuity can be diffused by viscosity; but at higher Re, the flow

becomes unstable even at moderate s. Magnaudet *et al.* (1995) have discussed this problem in detail in the context of axisymmetric strain and obtained the corresponding stability domain. In the present simulations for planar strain, we simply restrict computations to two values of s: one at $s = -0.04$ for $10 \leqslant Re \leqslant 300$ range and the other at $s = -0.1$ for $Re = 10$ only.

Contrary to elongational strain, the effect of compressional strain is to advance the location of separation and to increase the length of the recirculation region. Corresponding data are presented in table 4 and figure 8. Separation is found to advance more on the $x - y$ plane than on the $x - z$ plane. For example, at $Re = 50$ and $s = -0.04$, separation occurs at $\theta = 46.5^0$ and 45.5^0, respectively, on the $x-y$ and $x-z$ planes as opposed to 40.8^0 in uniform flow. Significant increase in the recirculation length is also clear from figure 8. At $Re = 50$ and $s = -0.04$, the length is 0.62, while it is 0.41 in uniform flow. The influence of compressional strain is to reduce the drag force. The drag coefficient for various Re is shown in figure 9. Since the strain magnitude is small, the only distinguishable change is for $Re \geqslant 200$ for which C_D is reduced by 11%. For the case of $Re = 10, s = -0.1$, a 20% decrease in C_D is observed (not shown in the figure).

Variation of $\langle C_P \rangle$ is shown in figure 11c for potential flow and for the case $Re = 300, s = -0.04$. Under compressional strain, the region of favorable pressure gradient is reduced. Decrease in pressure drop in the windward side is also faster compared to the uniform flow case. But unlike potential flow, $\langle C_P \rangle$ at $Re = 300$ is lower even on the downstream side of the sphere. Such decrease in $\langle C_P \rangle$ on the leeward side actually tends to increase the pressure drag. The effect is however overcome by the decrease in favorable pressure on the windward side resulting in an overall decrease in the pressure drag. Similar variation in $\langle C_P \rangle$ is observed at other Reynolds numbers as well. The average surface vorticity $\langle \omega_\phi \rangle$ for $Re = 10, s = -.1$ and $Re = 300, s = -0.04$ are shown in figure 12. The magnitude of $\langle \omega_\phi \rangle$ decreases on the downstream side and increases on the upstream side which results in a decrease in the viscous drag.

The $Re = 300, s = -0.04$ case develops unsteady vortex shedding and the time history of the drag coefficient is shown in figure 6. The shedding process appears to be more chaotic than in uniform flow and is dominated by a low frequency mode at $St \approx 0.035$. Although the compressional strain magnitude considered is weak, certain aspects of the flow, such as movement of the separation line and the recirculation length seem to fit the trend observed in elongational strain. On the other hand, the behavior of the drag coefficient cannot be extrapolated from the results of elongational strain. As observed by Magnaudet *et al.* (1995), the present approach becomes unstable for larger values of compressional strain. This raises an interesting question whether such ambient flow configuration is stable for extended period of time and whether the quasi-steady approach employed here is meaningful.

4.2.3 *Relative velocity along the plane of strain* ($\Theta \neq 0$ or $\pi/2$, $\Phi = 0$)

This section deals with the situation when relative velocity is in the plane of strain but not aligned along the elongational or compressional directions of strain. In particular, the case of $\Theta = \pi/4$, $\Phi = 0$ will be considered (see figure 4c). Along $x = 0$, $y > 0$ (the top side of the sphere), the straining flow acts in the same direction of the uniform flow, while along $x = 0$, $y < 0$ (the bottom side) it opposes the uniform flow. Thus $y > 0$ side will be called the high-speed side (marked as HSS) and $y < 0$ will be called the low-speed side (LSS). The effect of strain on the structure of the wake is described first. Streamlines constructed from the velocity field on the $x-y$ plane are shown in figure 13. For the given strain orientation, this plane is a plane of symmetry. The $Re = 10, s = 0.1$ case is shown in figure 13a. The symmetry of the flow about the $x - z$ plane is broken and the front and rear stagnation points are no longer located at the poles $\theta = 0$ and π. At higher Re, the shape of the wake is dramatically modified in the presence of strain. Figures 13b and 13c show the effect of increasing strain magnitude while Re is held fixed at 50. Even a relatively weak strain of $s = 0.05$ can be seen to visibly break the axisymmetric nature of the wake. The recirculation eddy is suppressed on the high-speed side while it is reduced in

Re	s	θ_s		stagnation point	
		$\phi = 0$	$\phi = \pi$	rear	front
10	0.1			19.2	174.3
50	0.05	41.86	37.9	7.1, on LSS	174.0
50	0.1	47.64			173.9
50	0.2	52.19			170.0
100	0.1	57.58	31.71	5.3, on LSS	173.9
200	0.1	65.66	47.94	10.6	174.2
300	0.1	69.76	54.67	19.9	174.5

TABLE 6. Location of the separation and stagnation points for $\Theta = \pi/4, \Phi = 0$ case.

size on the low-speed side. Fluid moving around the bottom of the sphere continues around the eddy and departs near the upper separation line and joins with the fluid from the high speed side. The recirculation eddy is nearly removed with increasing strain magnitude, as shown in the figure 13c for $Re = 50, s = 0.1$. At even higher strain magnitudes the separation eddy is completely suppressed. The effect of strain at higher Re is considered in figure 13d for $Re = 300, s = 0.1$. The deformation of the recirculation eddy is quite similar to the one shown in figure 13b. Comparing figures 13c and d, it may be claimed that suppression of the eddy is pushed up to higher strain magnitude as Re increases. At $Re = 300$, $s = 0.1$, the flow is steady thus suggesting that strain oriented at $\pi/4$ tends to inhibit the vortex shedding process.

Locations of separation on the $x-y$ plane are presented in table 6. For the case of $s = 0.1$, at all $Re \geqslant 100$, separation is advanced on the high-speed side ($\phi = 0$) and is delayed on the low-speed side ($\phi = \pi$). The effect of increasing s from 0 to 0.2 while keeping Re fixed at 50 is also shown in table 6. For a relatively weak strain, at $s = 0.05$, separation line remains a closed curve, though not axisymmetric. Separation on $\phi = 0$ occurs at $\theta = 41.9^0$ which is higher than $\theta = 40.8^0$ in uniform flow. Separation on $\phi = \pi$ is however delayed to $\theta = 37.9^0$. When s is increased beyond 0.05, lower separation no longer exists, and upper separation is advanced further upstream. Also shown in table 6 are the locations of the rear and front stagnation points. Owing to the symmetry of the applied strain field about the $x - y$ plane, these points are confined to this plane only. However, they are no longer located at $\theta = 0$ and π. For the entire range of Re and s, the front stagnation point is located nearly at the same θ on the high-speed side. The movement of the rear stagnation point is however very different. At $Re = 10$ and $Re \geqslant 200$ and $s = 0.1$, it is located on the high speed side. But at $Re = 50$, $s = 0.05$ and $Re = 100$, $s = 0.1$, it has moved towards the low speed side.

We also examine the sphere wake by means of the surface streamline plots in figure 14. For $Re = 50, s = 0.05$ case shown in figure 14a, a downward movement of the rear stagnation point (indicated as RS in the plot) away from the geometric pole ($\theta = 0$) is clearly visible. The top-bottom asymmetry in the wake is also quite evident here. Figure 14b shows the surface streamlines for $Re = 50$ and $s = 0.1$. The separation line is no longer a closed curve and it exists only on the

high-speed side. With further increase in s, the separation line is gradually reduced before being eliminated completely at a sufficiently high strain. The non-axisymmetric nature of the wake can also be observed in figures 14c and d corresponding to $Re = 100, s = 0.1$ and $300, s = 0.1$ cases.

A close observation of the surface streamlines reveals an interesting phenomenon. In figure 14a, for $Re = 50$ and $s = 0.05$, all the surface streamlines merge tangentially to the separation line at the upper singular point located on the $\phi = 0$ plane; whereas only two surface streamlines intersect each other at the lower singular point at $\phi = \pi$. Thus, the upper singular point is a nodal point, denoted by N in the plot, while the lower one is a saddle point, denoted by S. At $s = 0.1$ (figure 14b), the nodal point is no longer located at $\phi = 0$. Instead, there are two nodal points (N1 and N2) located on either side of the $x - y$ plane and a saddle point (S) appears at $\phi = 0$. The trend is further magnified at higher strain magnitudes. The effect of increasing Re is shown in the next two figures. At $Re = 100$ and $s = 0.1$, in figure 14c, the singular points at $\phi = 0$ and π are saddle points (S1 and S2). Two nodal points (N1 and N2) are now located away from the $x - y$ plane in $y < 0$. At $Re = 300, s = 0.1$, in figure 14d, two nodal points merge into the lower singular point (N) at $\phi = \pi$ while the upper singular point (S) at $\phi = 0$ still remains a saddle point.

The drag coefficient C_D for the case of $\Theta = \pi/4$ and $\Phi = 0$ is presented in figure 15a for $s = 0.1$. The coefficients C_D, C_{PD} and C_{VD} are nearly the same as their values in uniform flow. Although there is a small increase in the coefficients over their values in uniform flow, the effect is far less than what was observed under elongational alignment. Considering potential flow for the orientation $\Theta \neq 0$ and $\Phi = 0$, the velocity potential is given by

$$\left(\tilde{r} + \frac{1}{16\,\tilde{r}^2}\right)\cos\theta + s\left(\frac{\tilde{r}^2}{2} + \frac{1}{96\,\tilde{r}^3}\right)\left(\frac{3}{2}\cos^2\theta - \frac{1}{2}\right)\cos 2\Theta$$
$$-s\left(\frac{\tilde{r}^2}{2} + \frac{1}{96\,\tilde{r}^3}\right)\left[(\sin^2\theta\cos 2\phi)\cos 2\Theta + \sin 2\theta\cos\phi\sin 2\Theta\right] \tag{4.9}$$

In particular, for $\Theta = \pi/4$ and $\Phi = 0$, $C_{D,\mathrm{pot}} = 0$. Therefore the trend of weak influence on drag observed at finite Reynolds number is consistent with the potential flow result.

The ambient flow considered here is not symmetric about the $x-z$ plane. As a result, a lift force is generated along the y-direction. For $\Theta = \pi/4$, $C_{L,\mathrm{pot}} = 2s$, and the lift force is directed to the positive y-axis, i.e., from the low-speed side of the sphere to the high-speed side. In the limit of low Reynolds number ($Re \ll 1$) also, the lift coefficient is observed to be positive by Pérez-Madrid *et al.*(1990). The present simulations, however, show that C_L at moderate Re may be directed towards the negative y-axis. Variation of C_L and its pressure and viscous components are shown in figure 15b for a fixed strain magnitude of $s = 0.1$. Except for $Re < 40$, C_L is negative over the entire range of Re. The pressure contribution C_{PL} is negative for approximately $Re > 80$, while the viscous contribution C_{VL} is negative for $Re > 10$. The generation of a negative lift force at finite Re is contrary to the potential flow and low Reynolds number limits and therefore is somewhat surprising. However, it must be pointed out that such negative lift force has also been observed in both experiments and computations for the case of spheres subjected to a linear shear flow by Komori & Kurose (1999).

Figure 15c presents the variation of the lift coefficients with increasing s as Re is held fixed at 50. The finite Re behavior is very different from the linear variation predicted by potential flow. All three lift coefficients first attain a negative maximum at about $s = 0.05$. Both C_L and C_{PL} then increase with s and eventually become positive for $s > 0.1$. The viscous part C_{VL} however remains negative up to about $s = 0.25$. At $s = 0.05$, the viscous lift contributes to nearly 70% of the total lift, while at $s = 0.3$ it accounts for only 12%. Thus, the pressure contribution takes over the viscous contribution as Re and s increase.

Generation of the negative lift force is explained by considering separately the pressure and the

viscous contributions. The pressure coefficient C_P on the surface of the sphere is shown in figure 16 for two cases: $Re = 200$, $s = 0.1$ and $Re = 50$, $s = 0.2$. We consider the variation of C_P with θ along $\phi = 0$ and π where C_P attains extremum values. Corresponding distributions for potential flow are also shown. The potential pressure along the high-speed side is slightly larger than that along the low-speed side near $\theta = 0$ and π. However, a large drop in pressure along the high speed side near $\theta = \pi/2$ results in a positive lift. The finite Re behavior is significantly different, especially in the wake region. For $Re = 200, s = 0.1$ case, the pressure drop along the high speed side is much less and C_P along $\phi = 0$ and $\phi = \pi$ are nearly the same for $\theta \leqslant \pi/2$. On the other hand, for $\theta > \pi/2$, C_P along $\phi = 0$ is higher than that along $\phi = \pi$. Therefore the negative value of C_{PL} arises essentially from the negative contribution in $\theta > \pi/2$. In figure 16b, for the case of $Re = 50, s = 0.2$, the pressure drop on the high speed side near $\theta = \pi/2$ is large enough to overcome the negative contribution arising from the upstream side, thereby producing a positive value of C_{PL}.

In figure 15 it was observed that for moderate strain magnitudes in the range of $0 \leqslant s \leqslant 0.3$, pressure contribution to the lift force is generally positive at low Reynolds numbers ($Re = 10$) and negative at higher Reynolds numbers ($Re \geqslant 200$). In the intermediate Reynolds numbers ($Re = 50$), pressure contribution changes from negative at low strain values ($s \leqslant 0.1$) to positive at higher strain. This behavior is investigated further in figure 17 where contours of the local contribution to the y-component of the pressure lift is plotted. Here the local contribution is defined in terms of the deviation in the surface pressure from its surface-averaged value. Four different cases are considered: a) $Re = 10$, $s = 0.1$; b) $Re = 50$, $s = 0.05$; c) $Re = 50$, $s = 0.2$; and d) $Re = 300$, $s = 0.1$. Owing to the symmetry of the flow about the $x - y$ plane, only one half of the surface is shown. For all the cases, behavior near $\theta = \pi$ is similar to the potential flow result: higher than average pressure above the centerline contributing to negative lift and below average pressure below the centerline contributing to positive lift. The negative contribution above the centerline somewhat outweighs the positive contribution and thus for all the four cases there is a negative contribution to the pressure lift coming from the upstream portion of the sphere. However, away from the upstream side, results are markedly different for each case. For $Re = 10, s = 0.1$, a strong upward force is present on the downstream side which makes the resultant contribution to be positive. For $Re = 50, s = 0.05$ case, pressure on the upper surface is roughly comparable to that on the lower surface over almost entire θ except near $\theta = \pi$. Near $\theta = \pi$, negative contribution is strong enough to produce a negative pressure lift. When s is increased, as in figure 17c for $Re = 50, s = 0.2$, a stronger positive force acts on the top surface near $\theta = \pi/2$ resulting in a positive pressure lift. For the high Reynolds number case of $Re = 300, s = 0.1$ shown in figure 17d, significant pressure difference comes only from the upstream side of the sphere, and the overall pressure lift is negative.

In summary, one can conclude that when the recirculation region is absent in the wake, pressure distribution in $\theta \leqslant \pi/2$ dictates the pressure lift force to be positive, just as in potential flow. This situation arises at low Re when the recirculation region is entirely absent, or at higher Re, when the formation of the recirculation region is suppressed by the presence of a strong straining flow. When the recirculation region is present, the wake pressures above and below the $x - z$ plane are nearly equalized and the resultant effect is a negative pressure lift arising from the front part ($\theta \approx \pi$) of the sphere.

The viscous lift force arising from two contributions, $\tau_{r\theta}$ and $\tau_{r\phi}$, is listed in table 7. Contribution from $\tau_{r\phi}$ is negative over the entire range of Re and s. Contribution from $\tau_{r\theta}$ is mostly positive, but nearly an order of magnitude less than that from $\tau_{r\phi}$, except at $Re = 10$ and at $Re = 50$ for high values of s.

The role of the shear stress $\tau_{r\theta}$ to the lift force is examined in figure 18. The flow is from left to right and the view shown here is looking towards the negative z-axis. Here contours of the y-component of the viscous force arising from $\tau_{r\theta}$, i.e., $\tau_{r\theta} \cos\theta \cos\phi$, are shown on one half of

Re	s	C_{VL} due to $\tau_{r\theta}$	C_{VL} due to $\tau_{r\phi}$
10	0.1	0.0298	−0.03
50		0.0110	−0.04
100		0.0069	−0.04
200		0.0030	−0.03
300		0.0006	−0.02
50	0.05	−0.008	−0.06
	0.1	0.011	−0.04
	0.2	0.035	−0.04

TABLE 7. Contribution of the shear stresses $\tau_{r\theta}$ and $\tau_{r\phi}$ to viscous lift for the case $\Theta = 45^0, \Phi = 0$.

the sphere surface. A positive value of this quantity leads to a positive viscous lift force while negative value contributes negatively. We consider two representative cases: a) $Re = 200, s = 0.1$ and b) $Re = 50, s = 0.2$. For the first case, values on the upper and lower surface of the sphere are nearly comparable but of opposite sign over the entire range of θ. Thus the integrated value of $\tau_{r\theta} \cos\theta \cos\phi$ over the surface is negligible. For the second case, values on the upper and lower surface on the upstream side of the sphere are roughly the same and of opposite sign. But a positive contribution arises from the lower surface on the downstream side of the sphere. Similar to the surface pressure behavior, the effect of $\tau_{r\theta}$ is dictated by the presence of a recirculation eddy. In the case of $Re = 200, s = 0.1$, the presence of a recirculation region leads to a weaker $\tau_{r\theta}$ distribution on the leeward side. On the other hand, at $Re = 50, s = 0.2$, the recirculation eddy is suppressed and a strong flow gradient is created at the lower surface resulting in a larger and positive $\tau_{r\theta}$ contribution.

The persistent negative contribution from $\tau_{r\phi}$ is explained in figure 19. Contours of the local contribution to the viscous lift arising from $\tau_{r\phi}$, i.e., $-\tau_{r\phi} \sin\phi$ are shown for $Re = 200, s = 0.1$. A strong negative force acts almost over the entire surface. Generation of this downward force is due to the distribution of the azimuthal velocity component, u_ϕ, around the sphere. Figure 19b shows the contours of u_y velocity component on the $x - z$ plane. Note that in this plane u_ϕ is identically same as u_y. The u_y component is directed towards the negative y-axis around the sphere almost over the $x - z$ plane, except near the rear stagnation point. The contours of u_y are clustered closely on the upstream side than on the downstream side. As a result a strong negative gradient is generated over the upstream side of the sphere and a relatively weaker positive gradient is created over a smaller region on the downstream surface. Therefore, $-\tau_{r\phi} \sin\phi$ integrated over the entire surface leads to a negative contribution to the lift force.

4.2.4 *Effect of varying* Θ

The effect of varying the angle Θ is investigated in figure 20. We consider only the range $0 \leqslant \Theta \leqslant \pi/2$ and the results for $\pi/2 < \Theta < \pi$ can easily be obtained by the transformation $\Theta \to \Theta + \pi/2$. According to the potential flow result (4.9), the drag coefficient for such configuration is given by $2s \cos 2\Theta$ and the lift coefficient (directed towards the positive y-direction) by $2s \sin 2\Theta$. These results are compared with the simulation results for $Re = 10$, $s = 0.1$ and $Re = 50$, $s = 0.1$ cases. For both cases the trend of the pressure drag matches reasonably well with the potential flow result. For $\Theta < \pi/4$, the elongational part of the strain-rate tensor is more aligned with the direction of relative velocity and the drag coefficient is higher than in uniform flow. As Θ increases,

the compressional part of the strain-rate tensor becomes more aligned with relative velocity and results in a decrease in C_D.

The lift coefficients for the two cases are shown in figures 20c and d. The trend is somewhat complex and is dictated by the presence or absence of a recirculation eddy. The pressure contribution, C_{PL}, at $Re = 10$ is positive for all Θ with a maximum value at about $\Theta = \pi/4$ and thus follows the same trend as in potential flow. C_{VL} is negative in the range $\pi/4 < \Theta < \pi/2$ due to a negative contribution from $\tau_{r\phi}$, as discussed earlier. However, the pressure contribution outweighs the viscous contribution, and the total lift force remains positive at $Re = 10$ for all Θ.

At $Re = 50$, in figure 20d, we consider the range $0 \leqslant \Theta \leqslant 3\pi/8$, as $\Theta = \pi/2$ (pure compressional alignment) was found to be unstable (see §4.2.2). Unlike in potential flow, C_{PL} is not symmetric about $\Theta = \pi/4$ and it exhibits a peak around $\Theta = \pi/8$. Although positive in general, it tends to become negative at higher Θ where the compressional strain is increasingly aligned with relative velocity. Such behavior is again due to the presence of a recirculation region. For $\Theta < \pi/8$, the recirculation region is suppressed and the top-bottom asymmetry in the surface pressure leads to a positive C_{PL}. Above $\Theta = \pi/8$, a recirculation region starts developing which reduces the wake pressure difference above and below the $x - z$ plane and the pressure differential near the front stagnation point dominates, leading to a negative pressure lift. The viscous lift coefficient at $Re = 50$ is negative over the entire range of Θ. For $\Theta > \pi/6$, its magnitude is higher than the pressure lift coefficient resulting in a negative total lift force.

4.2.5 *Relative velocity away from the plane of strain*

In this section we will consider a strain orientation such that relative velocity is not on the plane of strain; in particular, the results for $\Theta = 0$ and $\Phi = \pi/4$ (figure 4d) are presented here. For an axisymmetric strain this configuration is same as $\Theta = \pi/4, \Phi = 0$. For a planar strain these two cases are very different in terms of the wake structure and the drag and lift forces. Here, the $x - z$ plane is a plane of symmetry, and streamlines constructed on this plane are shown in figure 21. Adjacent to the sphere, the ambient velocity is higher along $x = 0$, $z < 0$ and this side will be termed as the high-speed side while $x = 0$, $z > 0$ will be called the low-speed side. A word of caution is warranted in interpreting this figure - although in the vicinity of the sphere the effect of strain appears to move the fluid from top left to bottom right, the far field flow is consistent with what is shown in figure 4d.

In figure 21a, for $Re = 10, s = 0.1$, it is observed that the rear and front stagnation points move away from the geometric poles at $\theta = 0$ and π. The front stagnation point has moved toward the high speed side and the rear one has moved to the low speed side. At $Re = 50, s = 0.05$, in figure 21b, the wake is suppressed on the high speed side and reduced in size on the low speed side. As s is increased to 0.2 keeping Re fixed at 50, in figure 21c, the wake is completely suppressed. The case of $Re = 300, s = 0.1$ is shown in figure 21d. Suppression of the wake is now possible only at higher strain magnitudes. Comparing figure 21 with figure 13 it can be seen that the streamlines on the $x - z$ plane in case of $\Theta = 0$, $\Phi = \pi/4$ appear qualitatively similar to those on the $x - y$ plane in case of $\Theta = \pi/4$, $\Phi = 0$. However, quantitative differences exist between the two cases, for example, in terms of the location of the separation points. In general, at the same Re and s, deformation of the wake bubble is less for $\Theta = 0$, $\Phi = \pi/4$ than for $\Theta = \pi/4$, $\Phi = 0$. This can be clearly seen for $Re = 300, s = 0.1$ by comparing figures 13d and 21d.

Surface streamlines for the orientation $\Theta = 0, \Phi = \pi/4$ are shown in figure 22, and qualitative comparison with figure 14 can be drawn. At $Re = 50, s = 0.05$, in figure 22a, axisymmetric nature of the wake is broken and the rear stagnation point (denoted by RS in the figure) is seen to have shifted to the low speed side. Two saddle points (S1 and S2) are seen on the separation line along the $x - z$ plane, while two nodal points (N1 and N2) appear on both sides of the $x - z$ plane on the high speed side. When s is increased to 0.1, asymmetry about the $x - y$ plane is further enhanced as in figure 22b. Further increase in s to 0.2 causes the separation line to disappear on

the low speed side (figure 22c). The nodal points now have moved closer to the $x-z$ plane. The case of $Re = 300, s = 0.1$ is shown in figure 22d. The separation line now appears as a closed curve and the rear stagnation point has shifted to the high speed side. On the symmetry plane, a saddle point (S) exists on the high speed side and a nodal point (N) on the low speed side.

The velocity potential for the configuration $\Theta = 0$, $\Phi \neq 0$ is given by

$$\left(\tilde{r} + \frac{1}{16\tilde{r}^2}\right)\cos\theta + s\left(\frac{\tilde{r}^2}{2} + \frac{1}{96\tilde{r}^3}\right)\left(\frac{3}{2}\cos^2\theta - \frac{1}{2}\right)\cos^2\Phi$$
$$-s\left(\frac{\tilde{r}^2}{4} + \frac{1}{192\tilde{r}^3}\right)\left[(\sin^2\theta\cos 2\phi)(1+\sin^2\Phi) - (\sin 2\theta\,\sin\phi)\sin 2\Phi\right] \tag{4.10}$$

For $\Phi = \pi/4$, the above equation yields $C_{D,\mathrm{pot}} = s$. The corresponding finite Re results for are shown in figure 23. At $s = 0.1$, C_D is slightly lower than the uniform flow result over the entire range of Re. The effect of increasing s at $Re = 50$ is also shown in the figure. Unlike the potential flow result, C_D at finite Re does not vary linearly with s. It reaches a minimum at around $s = 0.1$ and then slowly increases. At $s = 0.3$, C_D is about 26% higher than the uniform flow result. From the streamline plots shown in figure 21 it can be inferred that till about $s = 0.1$, the presence of wake recirculation dictates the behavior of drag; during this process the drag force decreases. With further increase in strain, recirculation region is suppressed and potential flow behavior is somewhat mimicked.

Due to asymmetry in the ambient flow about the $x-y$ plane, a side-force is generated along the positive z-direction. This behavior is different from the potential flow result, which predicts a side-force of magnitude s, but directed along the negative z-direction. Here we will denote the side force coefficients by C_Z, $C_{Z,P}$ and $C_{Z,V}$ representing the total, pressure and viscous components, respectively. Variations of these coefficients for the finite Re case are shown in figure 24. When s is fixed at 0.1 and Re is varied, the coefficients are positive over the entire Re range. Although the flow field close to the sphere appeared to be qualitatively similar to the case of in-plane strain oriented at $\Theta = \pi/4$, $\Phi = 0$, by comparing figures 24 and 15, it can be realized that the effect of strain orientation on lift is quite different. Most importantly, for $\Theta = \pi/4$, $\Phi = 0$ case, the lift coefficient is an order of magnitude lower than the drag coefficient, whereas in figure 24, the side-force coefficient C_Z is significantly larger and can be as high as 30% of C_D.

The variation of $\langle C_P\rangle$ with θ is shown in figure 25a for potential flow and for $Re = 50$. In potential flow, asymmetry in $\langle C_P\rangle$ about $\theta = \pi/2$ increases with s contributing to higher drag, whereas, at finite Re, the behavior of drag is dictated by the presence or absence of a recirculation region in the wake. For $Re = 50$, $s \leqslant 0.1$, the presence of a recirculation region raises $\langle C_P\rangle$ on the downstream side which results in a lower drag compared to uniform flow. For $s > 0.1$, the recirculation region is suppressed and $\langle C_P\rangle$ on the downstream side is reduced which results in a higher drag.

Figures 25b and 25c show the pressure contours on the surface of the sphere for potential flow at $s = 0.1$ and for $Re = 50, s = 0.1$. Asymmetry in the surface pressure distribution about the $x-y$ plane is responsible for the z-force in both cases. The negative z-force in potential flow is primarily due to the dominant low pressure present on the high speed side. No such distinct low pressure region can be observed in figure 25c. On the upstream side, in figure 25c, pressure on the high speed side is higher than on the low speed side, while on the downstream side, pressure on the low speed side is higher. The positive contribution coming from the upstream side outweighs the negative contribution from the downstream side resulting in a positive side-force.

Similar to the pressure contribution, the viscous contribution to the z-force is also positive for the finite Re cases. While both $\tau_{r\phi}$ and $\tau_{r\theta}$ contribute to the z-force, the former accounts for nearly 80% and is examined in figure 25d for $Re = 50, s = 0.1$. Here contours of azimuthal velocity component u_ϕ are plotted on the $x-y$ plane and the view shown is looking along the

z-direction. Positive values of u_ϕ imply that it is directed from the plane of the paper into the positive z-direction. Except in the near-wake region, u_ϕ appears to be positive over the entire region around the sphere. Particularly, in the windward side, a strong positive gradient $\tau_{r\phi}$ exists which contributes positively to the viscous side-force.

4.2.6 *Effect of Varying* Φ

Finally we consider the effect of varying the angle Φ between relative velocity vector and the plane of strain. It is sufficient to consider the range $0 \leqslant \Phi \leqslant \pi/2$ and the results for $\pi/2 \leqslant \Phi \leqslant \pi$ can be obtained by the transformation $\Phi \to \Phi + \pi/2$. Drag and lift forces under varying Φ are shown in figure 26 for potential flow and for $Re = 50$ at $s = 0.1$. The potential flow solution (4.10) yields $C_{D,\mathrm{pot}} = 2s\cos^2\Phi$ and $C_{Z,\mathrm{pot}} = -s\sin 2\Phi$. The behavior of the finite Re drag and side-force coefficients are quite complex and markedly different from the potential flow results.

5. Conclusion

This paper is concerned with the effect of spatial non-uniformity in the undisturbed ambient flow on the forces acting on a spherical body. Using a simple scaling analysis, we have shown that the standard practice of neglecting the added-mass and history terms in case of heavy particles is valid provided particles are small compared to the flow scales or when the particle Reynolds number is small. However, when the particle size is comparable to the flow scales and the particle Reynolds number is of the order of unity or more, the added-mass and history terms arising from the gradients of the ambient flow is important. In this paper we present results from the numerical simulations of a planar straining flow superimposed on a nominally steady uniform flow past a stationary sphere. The numerical methodology used in this study employs a high-resolution Fourier-Chebyshev pseudo-spectral scheme. The investigation covers a particle Reynolds number range of 10 to 300, thus extending from a non-separated wake to a time-dependent three-dimensional flow field. The planar straining flow is characterized by three parameters: the strain magnitude s, and the angles Φ and Θ formed between relative velocity vector and the principal directions of the strain-rate tensor. A wide range of s, Θ and Φ is examined with a systematic comparison against the results of potential flow and finite Re axisymmetric straining flow.

The focus has been to study the effect of planar strain on the structure of the wake in an attempt to explain the drag and lift forces acting on the particle. Several important observations can be made:

(a) Planar strain, when its direction of elongation is aligned with the direction of relative velocity, stabilizes the wake flow and delays the onset of unsteadiness. With increasing strain magnitude, separation is delayed and the length of the recirculation region decreases. Elongational strain of sufficient magnitude completely suppresses the recirculating eddy. In this respect, both planar and axisymmetric strains have similar effect on the wake structure. Despite the three-dimensional nature of planar strain, the flow in the vicinity of the sphere is nearly axisymmetric as indicated by the surface streamlines. Also, in terms of the length of the recirculation eddy and the angle of separation, the planar and axisymmetric strains yield similar results.

(b) Under elongational alignment, both planar and axisymmetric strain enhance the drag force. According to potential flow theory, strain induced increase in drag is given by $2s$ and is independent of the nature of strain. In case of axisymmetric strain, above a certain Re, increase in pressure drag very nearly follows the potential flow prediction. In case of planar strain, increase in pressure drag is still linear with s, but the rate of increase is higher. In both planar and axisymmetric strain, the viscous drag also increases with s, thus the increase in total drag is higher than the potential prediction. At low Re, increase in viscous drag is higher for planar strain; however, for $Re \geqslant 50$, the viscous drag is nearly the same for both cases.

(c) In potential flow, strain introduces a fore-aft asymmetry about $\theta = \pi/2$ contributing to

drag. At finite Re, the region of favourable pressure gradient extends into the leeward side of the sphere. Nevertheless, the wake pressure decreases resulting in further enhancement of the pressure drag. The drop in wake pressure is higher for planar strain.

(d) There are two mechanisms by which the surface vorticity distribution is modified under the influence of strain and leads to an increase in the viscous drag. First, in addition to the uniform flow, the imposed straining flow must also satisfy no-slip condition. This leads to an enhancement of surface vorticity on the downstream side and reduction on the upstream side. Secondly, the vortex stretching mechanism also leads to similar modification in surface vorticity. The resultant effect is an increase in the viscous drag.

(e) When compressional direction of strain is aligned with relative velocity, the extent of favourable pressure gradient on the upstream side is reduced and the recirculation region increases in size. Both the pressure and viscous drag components decrease compared to the uniform flow result. Results for compressional alignment ($s < 0$) cannot be extrapolated directly from those of elongational alignment ($s > 0$). Compressional alignment promotes unsteady vortex shedding in the wake and even a modest magnitude of strain renders the flow highly unstable. The instability arises from the discontinuity in the vorticity distribution across a stagnation plane located downstream of the sphere.

(f) Planar strain oriented at an angle other than a pure elongational or compressional alignment breaks the axisymmetric nature of the wake. The recirculation eddy is significantly deformed and the separation line with associated critical points on the surface of the sphere undergoes complex changes with increasing strain magnitude. For the case of $\Theta = \pi/4$, $\Phi = 0$ considered in detail, the recirculation region is completely suppressed at sufficiently high strain, and the strength of strain required for complete suppression increases with Re.

(g) For $\Theta = \pi/4$, $\Phi = 0$ configuration, the drag force is nearly the same as in uniform flow, in accordance with the potential flow result. However, unlike potential flow where the lift is always positive and increases linearly with the strain magnitude, at finite Re, the lift force shows a non-monotonic behavior and can be negative. The negative lift force can be related to the presence of a recirculation region in the wake. At higher strain magnitudes, when the recirculation region is suppressed, potenatil flow behavior is approximately recovered and the lift force becomes positive.

(h) The out-of-plane strain orientation $\Theta = 0$, $\Phi = \pi/4$ is found to yield markedly different results from the in-plane orientation $\Theta = \pi/4$, $\Phi = 0$ in terms of the flow structure and forces. In case of axisymmetric strain these two configurations are identical. The drag force is higher than the uniform flow result but not linear with s as predicted by the inviscid theory. Under $\Theta = 0$, $\Phi = \pi/4$ orientation, symmetry of the flow is broken and as a result there is a side force. The side force is opposite in sign to that predicted by the potential theory and its variation with strain magnitude is not linear.

(i) In general, for varying Θ and Φ, the present results show that at low Re (e.g. $Re \approx 10$) and for high strain magnitude in the absence of a recirculation eddy, the finite Re drag and lift forces somewhat follow the pattern observed in potential flow. At higher Reynolds numbers, their behavior is dictated by the presence of an eddy and thus may be very complex in nature.

The research is supported by the ASCI Center for Simulation of Advanced Rockets at the University of Illinois at Urbana-Champaign under the auspices of the U.S. Department of Energy through the University of California subcontract number B341494. Computational facilities from the National Center for Supercomputing Applications, UIUC are greatly acknowledged. Special thanks are due to Drs. J.P. Ferry and F. M. Najjar.

REFERENCES

ACHENBACH, E. 1974 Vortex shedding from spheres. *J. Fluid Mech.* **62**, 209–221.

ASHURST, W. T., KERSTEIN, A. R., KERR, R. M. & GIBSON, C. H. 1987 Alignment of vorticity and scalar gradient with strain rate in simulated Navier-Stokes turbulence. *Phys. Fluids* **30**, 2343.

ASMOLOV, E. S. 1999 The inertial lift on a spherical particle in a plane Poiseuille flow at large channel Reynolds number. *J. Fluid Mech.* **381**, 63–87.

AUTON, T. R. 1987 The lift force on a spherical body in a rotational flow. *J. Fluid Mech.* **183**, 199–218.

AUTON, T. R., HUNT, J. C. R. & PRUD'HOMME, M. 1988 The force exerted on a body in inviscid unsteady non-uniform rotational flow. *J. Fluid Mech.* **197**, 241–257.

BALACHANDAR, S. 1992 Structure in turbulent thermal convection. *Phys. Fluids A* **4**, 2715–2726.

BEDEAUX, D. & RUBI, J. M. 1987 Drag on a sphere moving slowly through a fluid in elongational flow. *Physica* **144A**, 285–298.

CLIFT, R., GRACE, J. R. & WEBER, M. E. 1978 Bubbles, Drops and Particles. Academic.

DANDY, D. S. & DWYER, H. A. 1990 A sphere in shear flow at finite Reynolds number: effect of shear on particle lift, drag and heat transfer. *J. Fluid Mech.* **216**, 381–410.

DENNIS, S. C. R. & WALKER, J. D. A. 1971 Calculation of the steady flow past a sphere at low and moderate Reynolds numbers. *J. Fluid Mech.* **48**, 771–789.

ELGHOBASHI, S. E. & TRUESDELL, G. C. 1992 Direct simulation of particle dispersion in decaying isotropic turbulence. *J. Fluid Mech.* **242**, 655.

HARPER, E. Y. & CHANG, I.D. 1968 Maximum dissipation resulting from lift in a slow viscous shear flow. *J. Fluid Mech.* **33**, 209–225.

HERRON, I. H., DAVIS, S. H. & BRETHERTON, F. P. 1975 On the sedimentation of a sphere in a centrifuge. *J. Fluid Mech.* **68**, 209–234.

HOGG, A. J. 1994 The inertial migration of non-neutrally buoyant spherical particles in two-dimensional shear flows. *J. Fluid Mech.* **272**, 285–318.

JOHNSON, T. A. & PATEL, V. C. 1999 Flow past a sphere up to a Reynolds number of 300. *J. Fluid Mech.* **378**, 19–70.

KIM, I., ELGHOBASHI, S. & SIRIGNANO, W. A. 1998 On the equation for spherical-particle motion: effect of Reynolds and acceleration numbers. *J. Fluid Mech.* **367**, 221–254.

KUROSE, R. & KOMORI, S. 1999 Drag and lift forces on a rotating sphere in a linear shear flow. *J. Fluid Mech.* **384**, 183–206.

LE CLAIR, B. P., HAMIELEC, A. E. & PRUPPRACHER, H. R. 1970 A numerical study of the drag on a sphere at low and intermediate Reynolds numbers. *J. Atmos. Sci.* **27**, 308–315.

LOVALENTI, P. M. & BRADY, J. F. 1993 The force on sphere in a uniform flow with small-amplitude oscillations at finite Reynolds number. *J. Fluid Mech.* **256**, 607–614.

MAGARVEY, R. H., & BISHOP, R.L. 1961 Transition ranges for three-dimensional wakes. *Can. J. Phys.* **39**, 1418–1422.

MAGNAUDET, J., RIVERO, M. & FABRE, J. 1995 Accelerated flows past a rigid sphere or a spherical bubble. Part 1. Steady straining flow. *J. Fluid Mech.* **284**, 97–135.

MAXEY, M.R. & RILEY, J. J. 1983 Equation of motion for a small sphere in a nonuniform flow. *Phys. Fluids* **26**, 883–889.

MCLAUGHLIN, J. B. 1991 Inertial migration of a small sphere in linear shear flows. *J. Fluid Mech.* **224**, 261–274.

MCLAUGHLIN, J. B. 1993 The lift on a small sphere in wall-bounded linear shear flows. *J. Fluid Mech.* **246**, 249–265.

MEI, R. & ADRIAN, R. J. 1992 Flow past a sphere with an oscillation in the free-stream and unsteady drag at finite Reynolds number. *J. Fluid Mech.* **237**, 133–174.

MERILEES, P. E. 1973 A pseudospectral approximation applied to the shallow water equation on a sphere. *Atmosphere* **11**, 13–20.

MITTAL, R. 1999 A Fourier Chebyshev spectral collocation method for simulation flow past spheres and spheroids. To appear in *Int. J. Numer. Meths. Fluids.*

MITTAL, R. & BALACHANDAR, S. 1996 Direct numerical simulation of flow past elliptic cylinders. *J. Comp. Phys.* **124**, 351–367.

MIYAZAKI, K., BEDEAUX, D. & AVALOS, J. B. 1995 Drag on a sphere in slow shear flow. *J. Fluid Mech.* **296**, 373–390.

NATARAJAN, R. & ACRIVOS, A. 1993 The instability of the steady flow past spheres and disks. *J. Fluid Mech.* **254**, 323–344.

ORSZAG, S. A. 1974 Fourier series on spheres. *Mon. Weather Rev.* **102**, 56–75.

PÉREZ-MADRID, A., RUBÍ, J. M. & BEDEAUX, D. 1990 Motion of a sphere through a fluid in stationary homogeneous flow. *Physica A* **163**, 778–790.

SAFFMAN, P. G. 1965 The lift on a small sphere in a slow shear flow. *J. Fluid Mech.* **22**, 385–400. (Corrigendum, 1968, **31**, 624).

SAKAMOTO, H. & HANIU, H. 1990 A study on vortex shedding from spheres in a uniform flow. *Trans. ASME: J. Fluids Engng.* **112**, 386–392.

SAKAMOTO, H. & HANIU, H. 1995 The formation mechanism and shedding frequency of vortices from a sphere in uniform shear flow. *J. Fluid Mech.* **287**, 151–171.

SCHONBERG, J. F. & HINCH, E. J. 1989 Inertial migration of a sphere in Poiseuille flow. *J. Fluid Mech.* **203**, 517–524.

SHARIFF, K. 1993 Comment on "Coordinate singularities" by P.R. Spalart. Unpublished.

SQUIRES, K. D. & EATON, J. K. 1991 Measurements of particle dispersion from direct numerical simulations of isotropic turbulence. *J. Fluid Mech.* **226**, 1–35.

STONE, H. A. 2000 Philip Saffman and viscous flow theory. *J. Fluid Mech.* **409**, 165–183.

TAYLOR, G. I. 1928 The forces on a body placed in a curved or converging stream of fluid. *Proc. R. Soc. Lond.* A **120**, 260.

TOBAK, M. & PEAKE, D. J. 1982 Topology of three-dimensional separated flows. *Ann. Rev. Fluid Mech.* **14**, 61–85.

TOLLMIEN, W. 1938 Uber krafte und momente in schwach gekrummten oder konvergenten stromungen. *Ing.-Arch.* **9**, 308.

TOMBOULIDES, A. G., ORSZAG, S. A. & KARNIADAKIS, G. E. 1993 Direct and large-eddy simulation of axisymmetric wakes. *AIAA Paper* 93-0546.

VOINOV, V. V., VOINOV, O. V. & PETROV, A. G. 1973 Hydrodynamic interactions between bodies in a perfect incompressible fluid and their motion in non-uniform streams. *Prikl. Math. Mekh.* **37**, 680.

WANG, L.-P. & MAXEY, M. R. 1993 Settling velocity and concentration distribution of heavy particles in homogeneous isotropic turbulence. *J. Fluid Mech.* **256**, 27–68.

WEISENBORN, A. J. 1985 Drag on a sphere moving slowly in a rotating viscous fluid. *J. Fluid Mech.* **153**, 215–227.

YEE, S. Y. K. 1981 Solution of Poisson's equation on a sphere by truncated double Fourier series. *Mon. Weather Rev.* **109**, 501–505.

ZHOU, J., ADRIAN, R. J., BALACHANDAR, S. & KENDALL, T. M. 1999 Mechanism for generating coherent packets of hairpin vortices in near wall turbulence. *J. Fluid Mech.* **387**, 353–396.

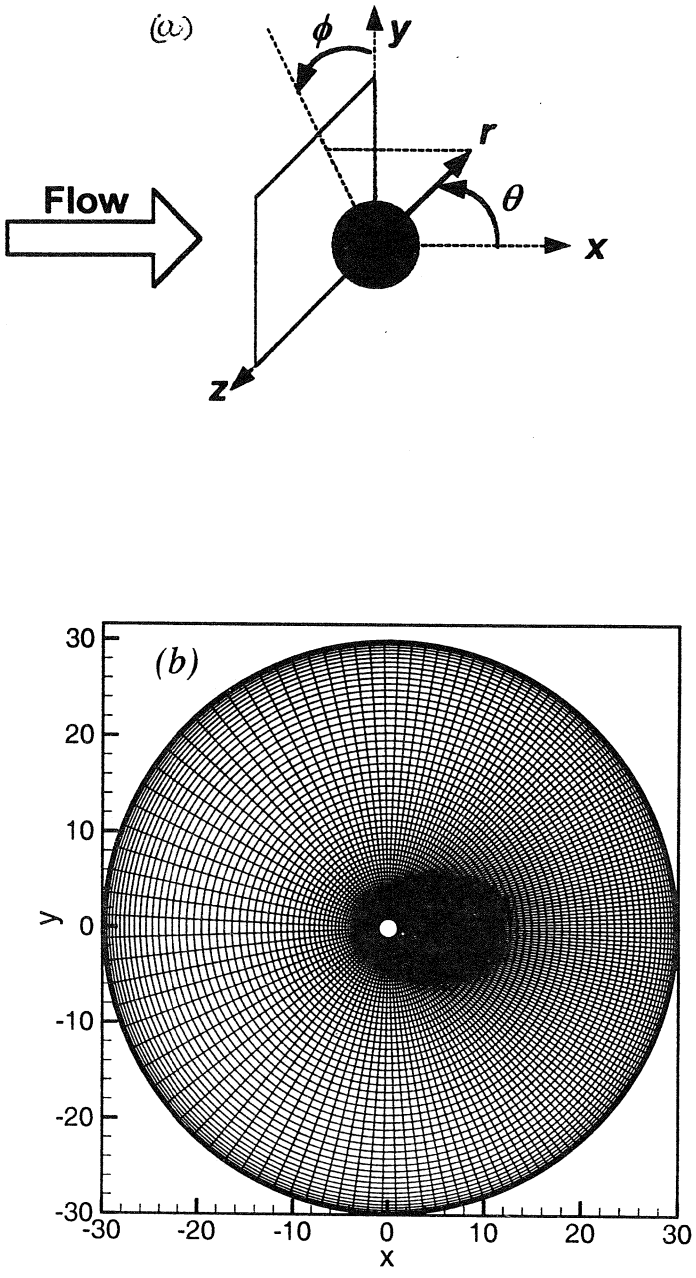

FIGURE 1. a) Schematic of the spherical coordinate and b) a ϕ-projection of the computational grid.

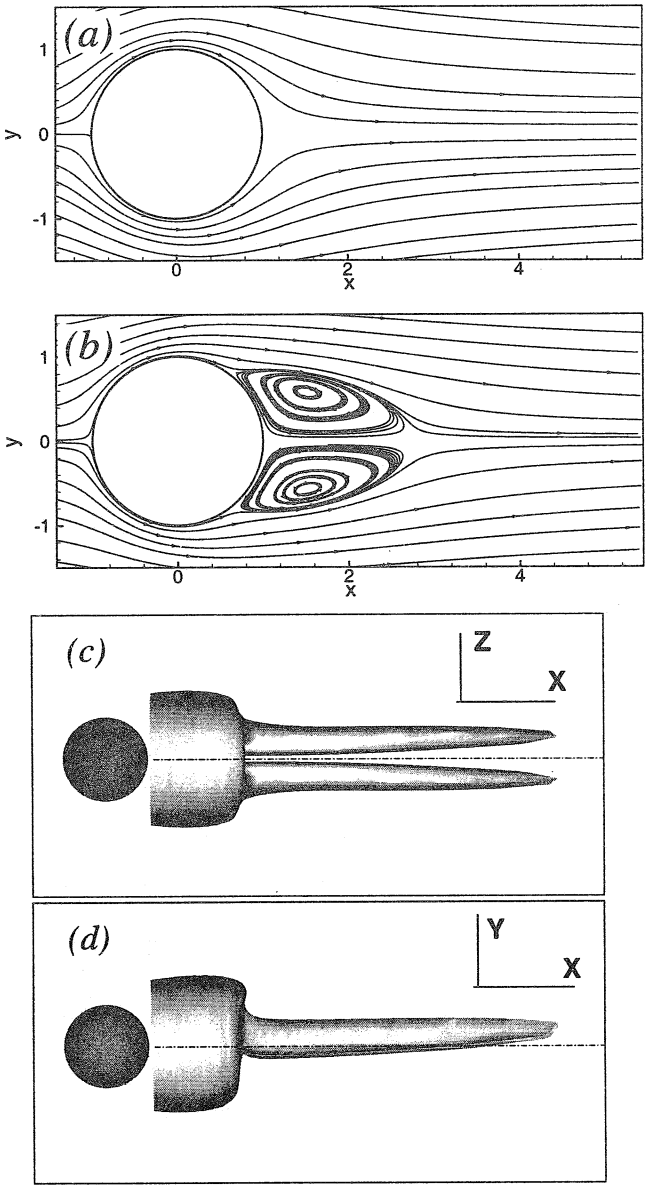

FIGURE 2. See next page

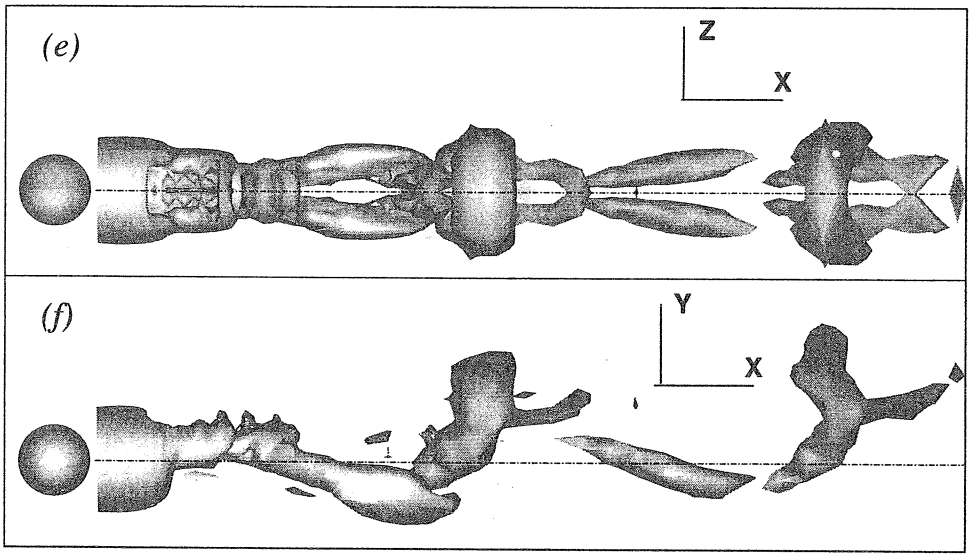

FIGURE 2. Wake structure in uniform flow. a) Streamlines at $Re = 10$ and b) $Re = 100$. Vortical topology at $Re = 250$: c) view along the plane of symmetry, d) view normal to the plane of symmetry. $Re = 350$: e) view along the plane of symmetry, f) view normal to the plane of symmetry.

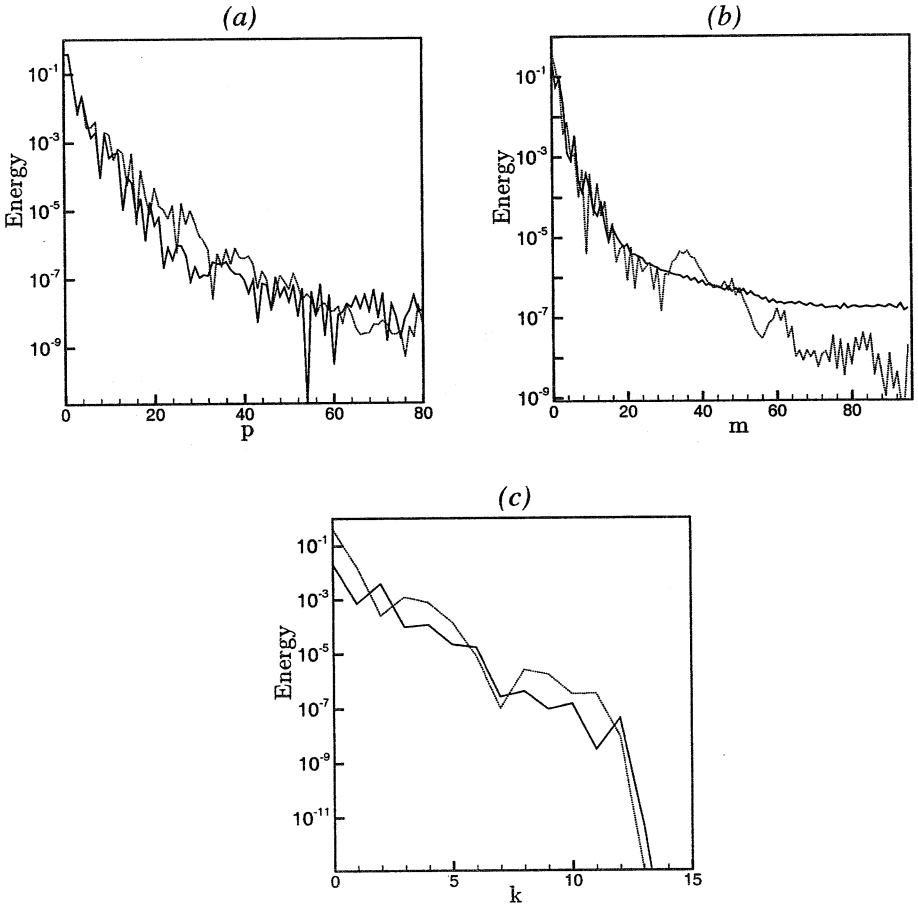

FIGURE 3. Energy spectra along three coordinate directions. a) Radial spectra at : $\theta = .07\pi$, $\phi = 0$ ——; and at $\theta = .14\pi$, $\phi = \pi$ · · · · ·. b) θ-spectra at : $r = 0.75d$, $\phi = 0$ ——-; and at $r = 10d$, $\phi = \pi$ · · · · ·. c) ϕ-spectra at : $r = 0.75d, \theta = .07\pi$ ——-; and at $r = 10d$, $\theta = .02\pi$ · · · · ·.

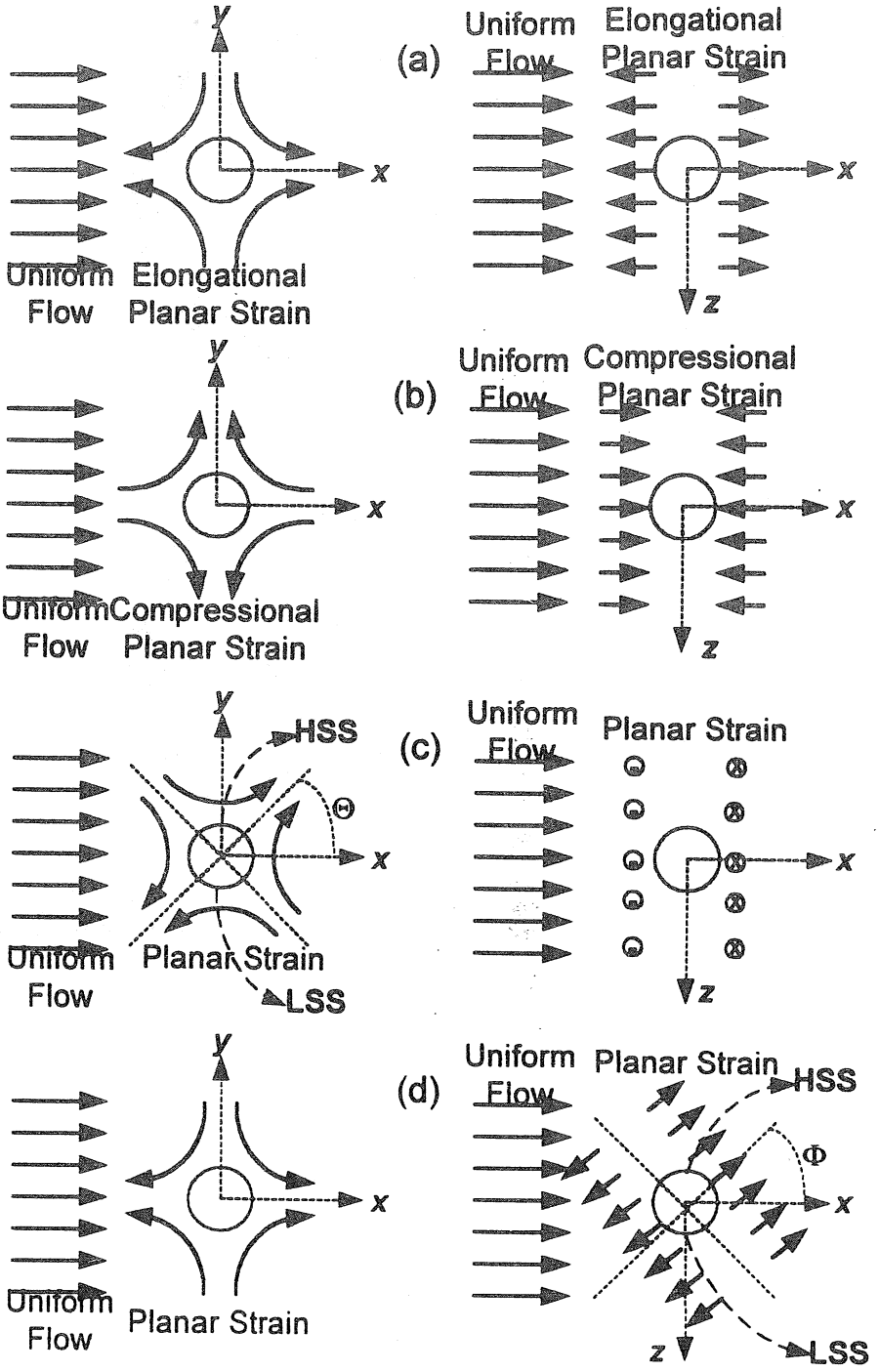

FIGURE 4. Schematic of strain orientation

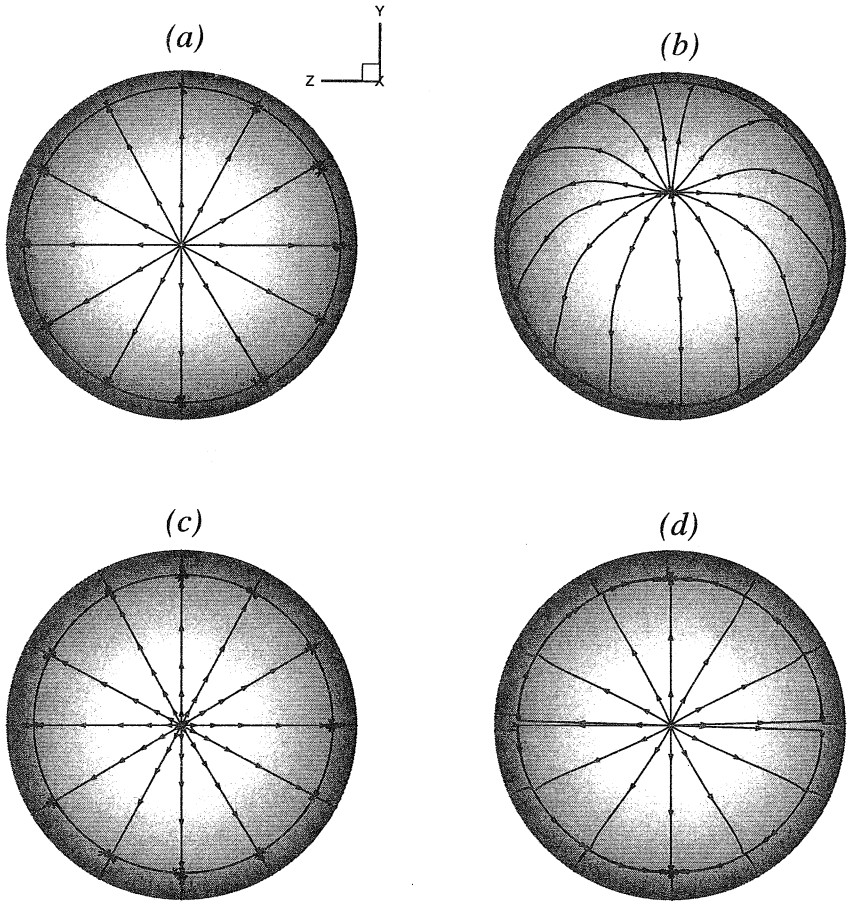

FIGURE 5. Surface streamlines for a uniform flow at a) $Re = 200$, and b) $Re = 300$. c) Axisymmetric strain at $Re = 300$ and $s = 0.1$, d) planar strain at $Re = 300$ and $s = 0.1$. Flow is directed from the plane of the paper.

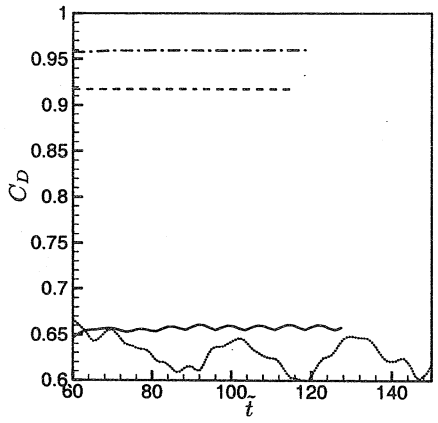

FIGURE 6. Time history of the drag coefficient at $Re = 300$: —— uniform flow; - - - - - -, axisymmetric strain at $s = 0.1$; - · - · - · - , elongational planar strain at $s = 0.1$; · · · · · , compressional planar strain at $s = -0.04$.

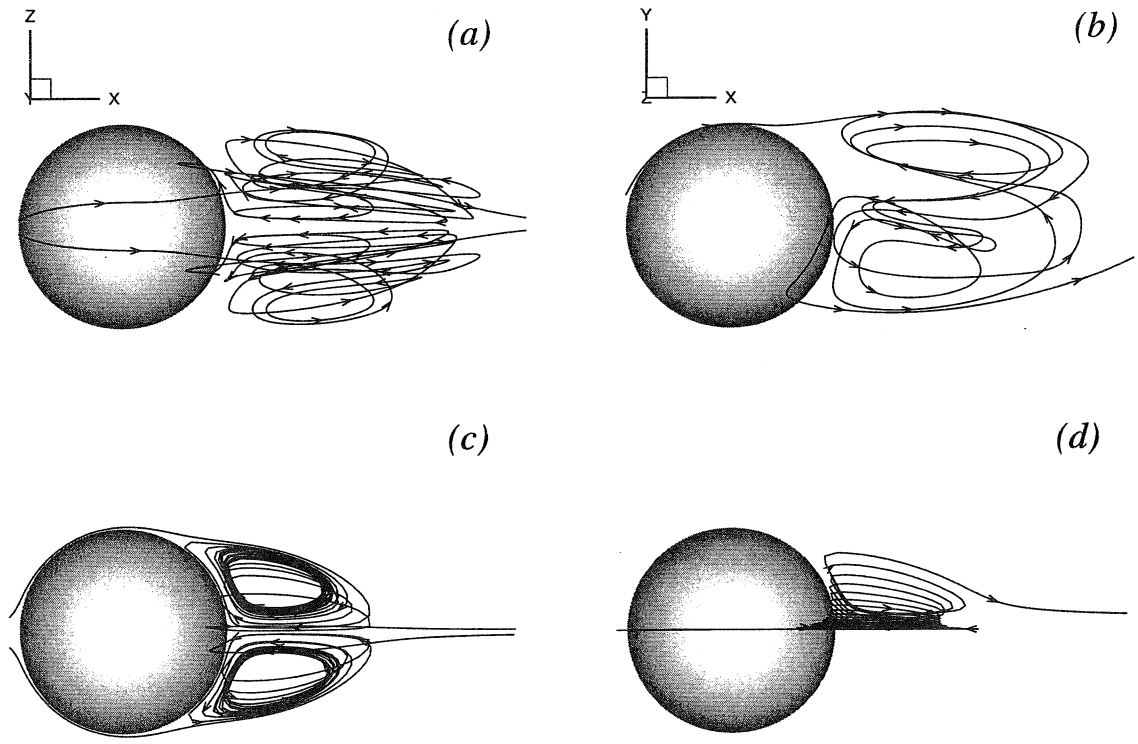

FIGURE 7. Fluid trajectory for uniform flow at Re = 300 (a and b) and planar strain flow at $Re = 300$ and $s = 0.1$ (c and d). The left panel shows the view along the $x - y$ plane, and the right panel shows the view along the $x - z$ plane.

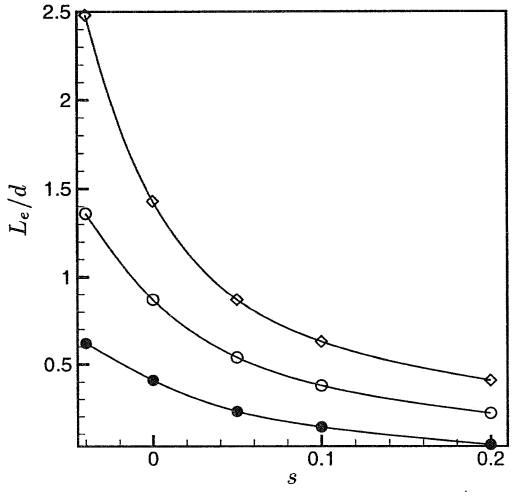

FIGURE 8. Separation length in planar strain : •, $Re = 50$; ○, $Re = 100$; ◇, $Re = 200$.

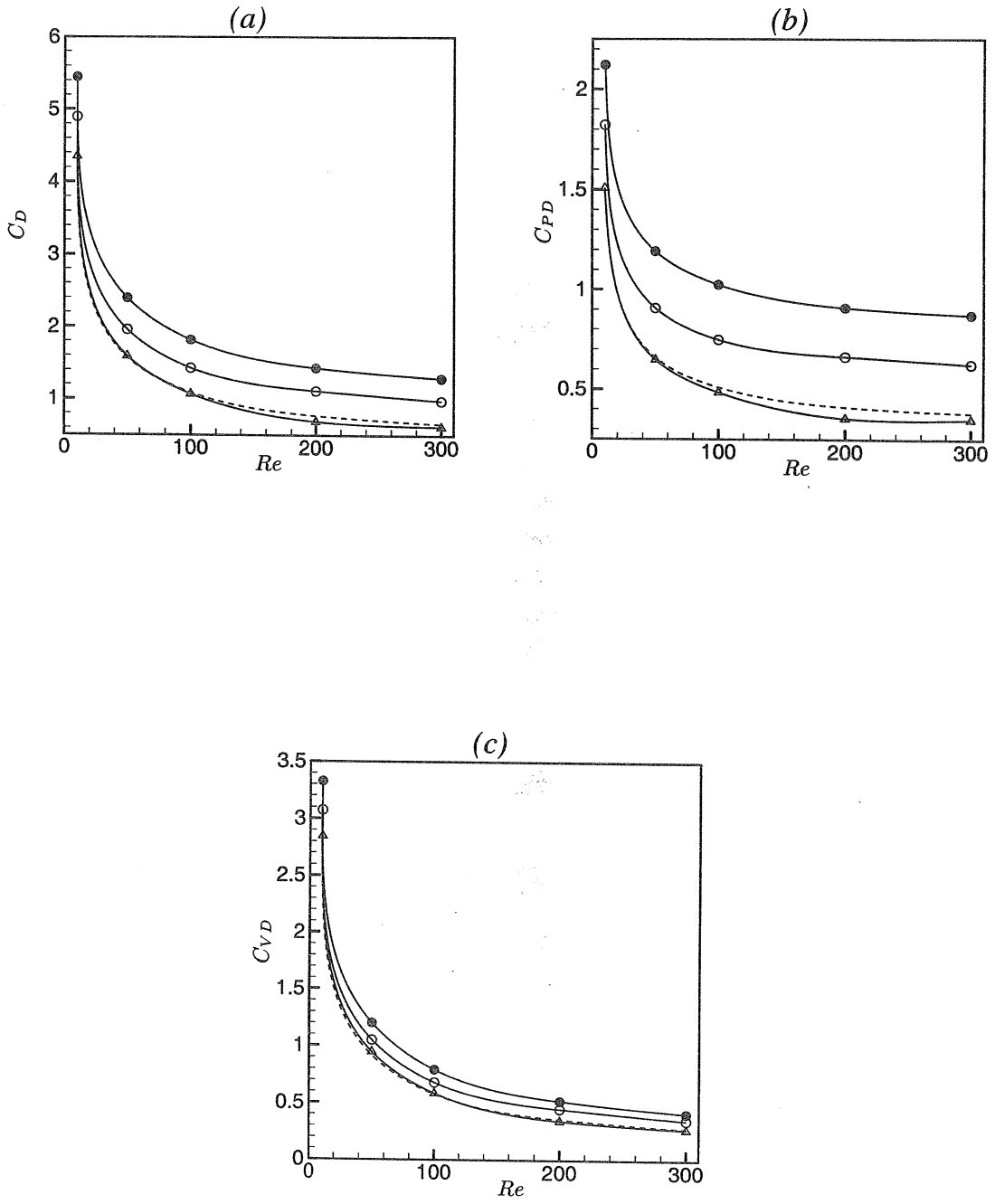

FIGURE 9. Variation of the drag coefficients with Re and s for planar strain at $\Theta = 0$ or $\pi/2$, $\Phi = 0$. a) C_D; b) C_{PD}; and c) C_{VD}. - - - -, uniform flow; —o—, elongational strain at $s = 0.1$; —●—, $s = 0.2$; —△—, compressional strain at $s = -0.04$.

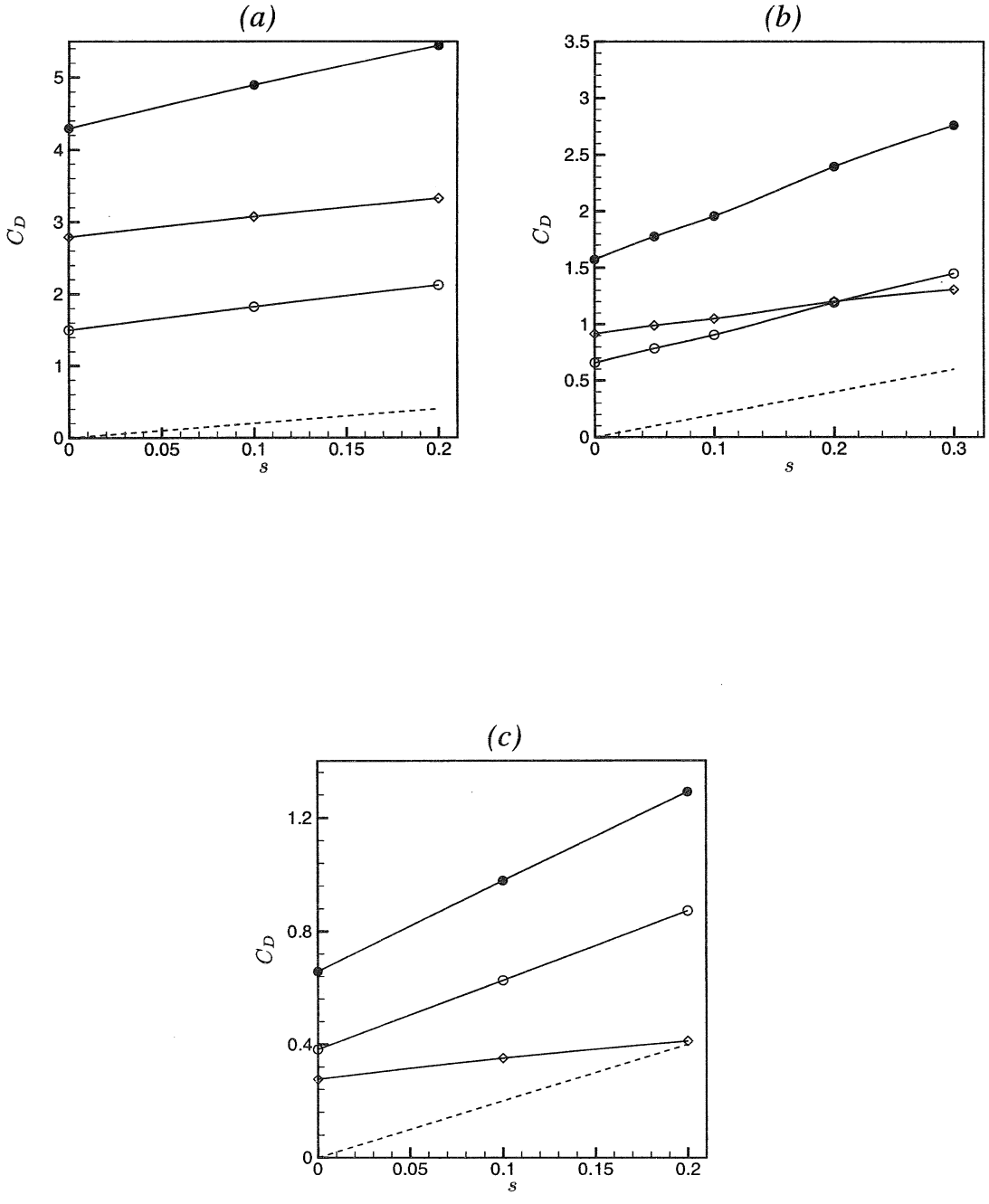

FIGURE 10. Variation of the drag coefficients with s for planar strain at $\Theta = 0$, $\Phi = 0$ a) $Re = 10$; b) $Re = 50$; c) $Re = 300$. —•—, C_D; —○—, C_{PD}; —◇—, C_{VD}; - - - -, potential flow result.

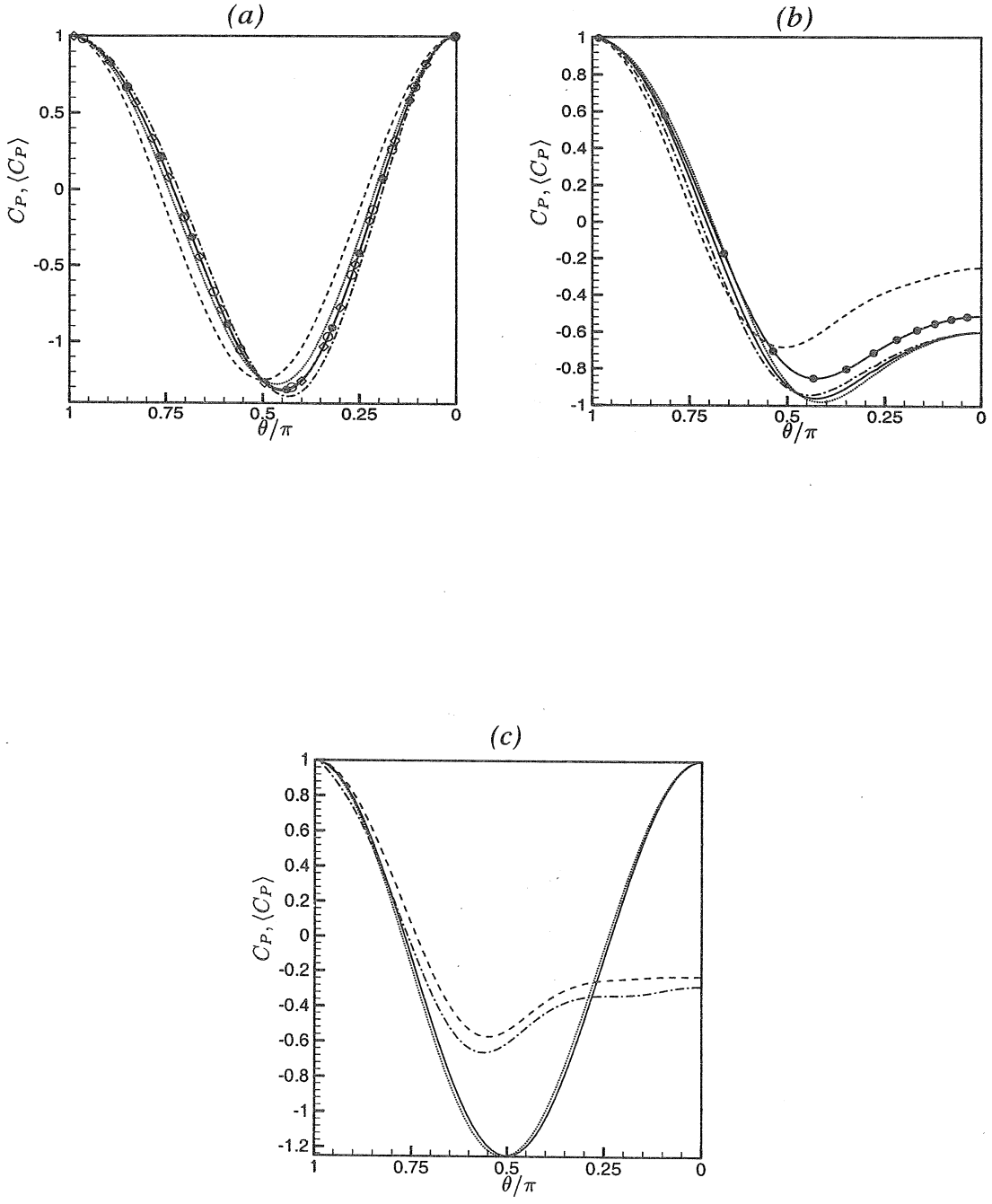

FIGURE 11. a) and b) : surface pressure distribution for the case $\Theta = 0$, $\Phi = 0$. a) Potential flow solutions : - - - -, uniform flow ($s = 0.0$); —○—, axisymmetric strain at $s = 0.2$; —●—, ϕ-average surface pressure $\langle C_P \rangle$ in planar strain at $s = 0.2$; C_P at different ϕ-locations in planar strain : -·-·- -, $\phi = 0$; —◇—, $\phi = \pi/4$; · · · · ·, $\phi = \pi/2$. b) $Re = 100$: - - - -, uniform flow ($s = 0.0$) ; —●—, axisymmetric strain at $s = 0.2$; ——, $\langle C_P \rangle$ for planar strain ($s = 0.2$) ; · · · · ·, C_P along $\phi = 0$ and -·-·-, C_P along $\phi = \pi/2$ in planar strain. c) compressional strain : ——, potential flow, $s = 0.0$; · · · · ·, potential flow at $s = -0.04$; - - - -, $Re = 300$, $s = 0.0$; -·-·-, $Re = 300$, $s = -0.04$.

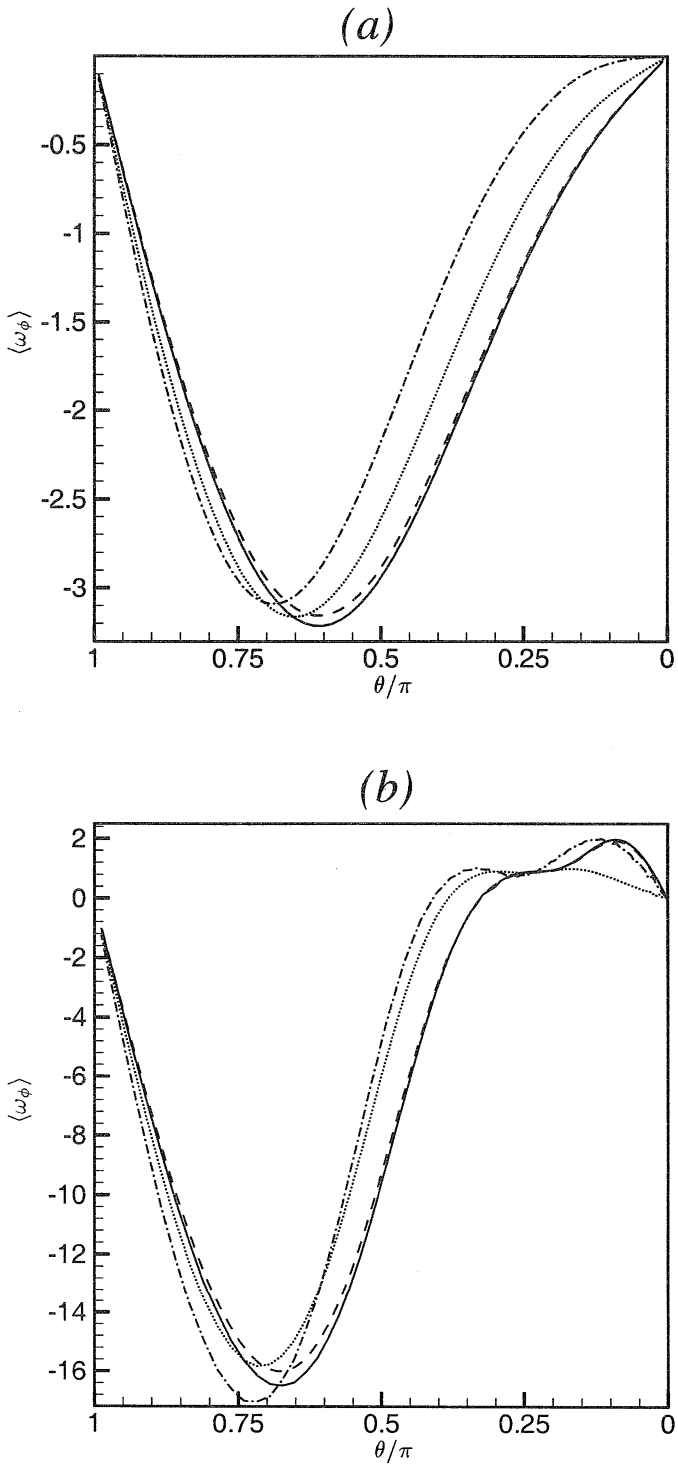

FIGURE 12. ϕ-averaged surface vorticity distribution for a) $Re = 10$ and b) $Re = 300$: · · · · ·, uniform flow ($s = 0.0$); - - - -, axisymmetric strain at $s = 0.1$; ——, planar strain at $s = 0.1$; -·-·-·-, compressional planar strain at $s = -0.1$ (for $Re = 10$) and $s = -0.04$ (for $Re = 300$).

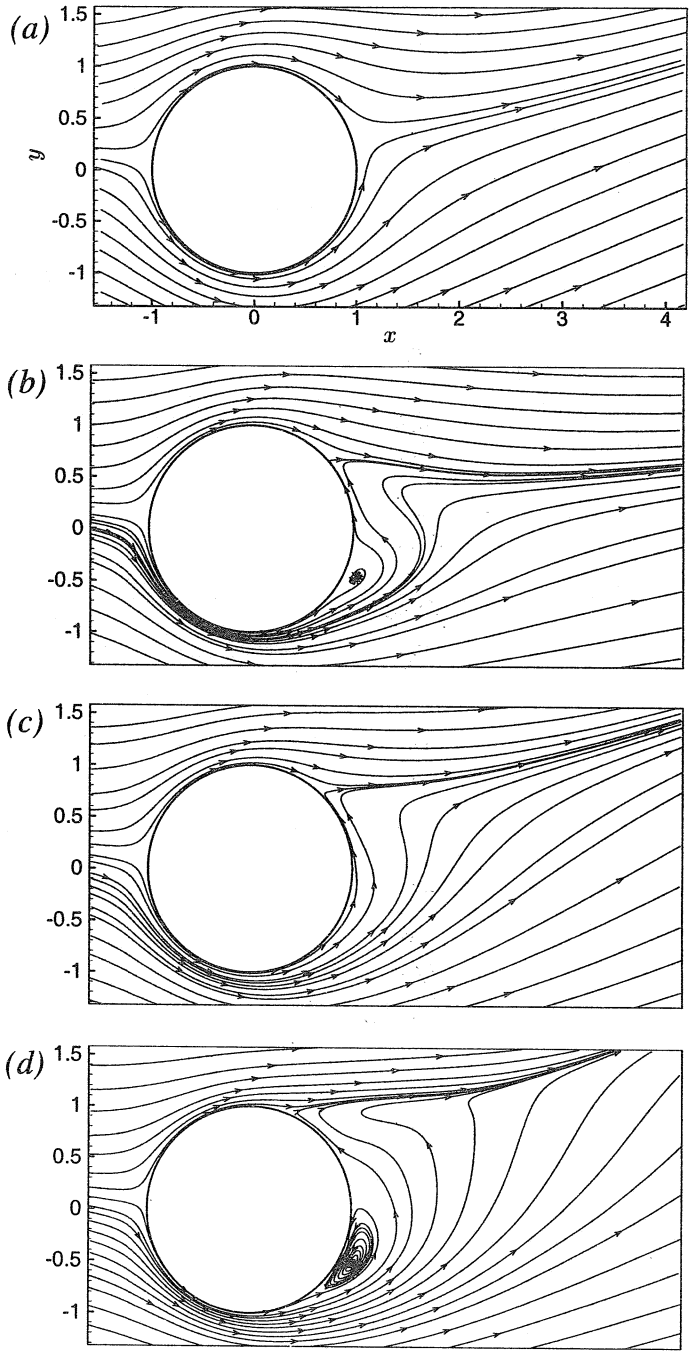

FIGURE 13. Streamline contours on the $x-y$ plane for $\Theta = \pi/4$, $\Phi = 0$. a) $Re = 10, s = 0.1$; b) $Re = 50, s = 0.05$; c) $Re = 50, s = 0.1$; d) $Re = 300, s = 0.1$.

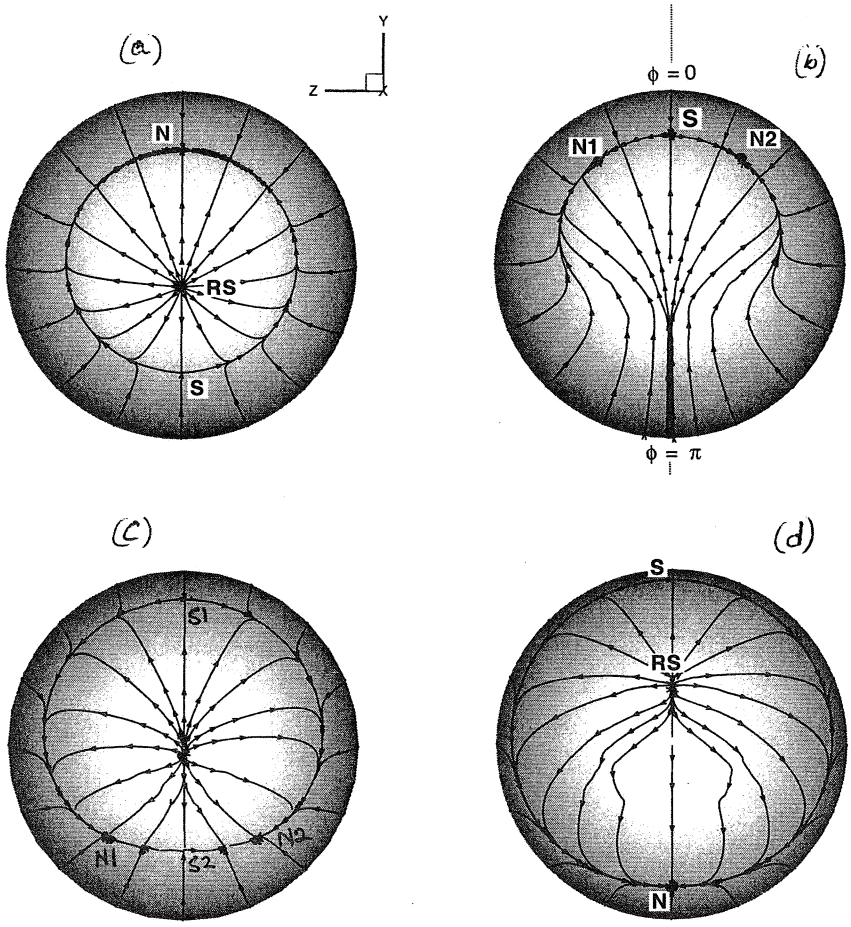

FIGURE 14. Surface streamlines for $\Theta = \pi/4$, $\Phi = 0$. a) $Re = 50, s = 0.05$; b) $Re = 50, s = 0.1$; c) $Re = 100, s = 0.1$; d) $Re = 300, s = 0.1$.

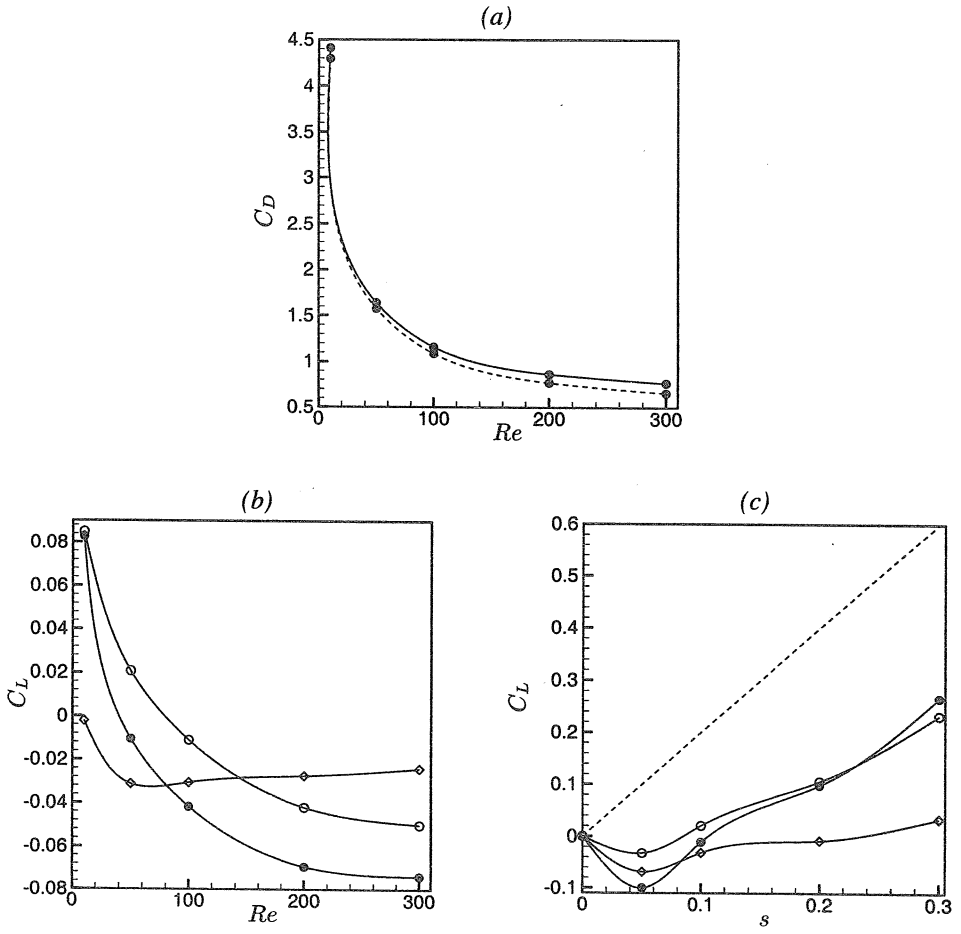

FIGURE 15. Drag and lift coefficients for $\Theta = 45^0, \Phi = 0$. a) Variation of C_D with Re : —●—, $s = 0.1$; - - ● - -, strain-free uniform flow. b) Lift coefficients at $s = 0.1$ and c) lift coefficients at $Re = 50$. ●, C_L ; ○, C_{PL} ; ◇, C_{VL}. - - - - - -, potential flow result.

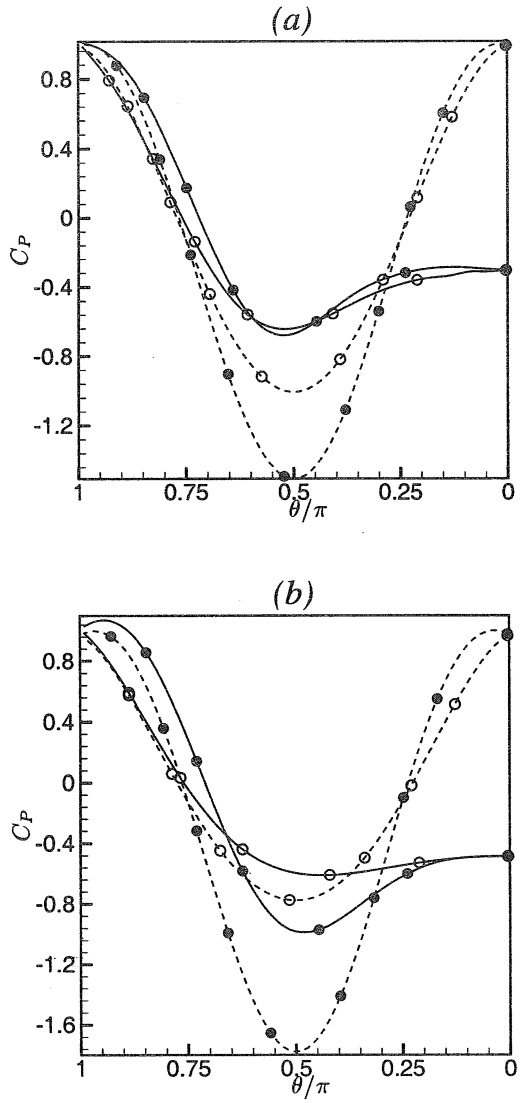

FIGURE 16. Surface pressure distribution for $\Theta = 45^0, \Phi = 0$ case. a) $Re = 200, s = 0.1$; b) $Re = 50, s = 0.2$. ——, finite Re result. - - - - - -, potential flow. • C_P along $\phi = 0$; ∘, C_P along $\phi = \pi$.

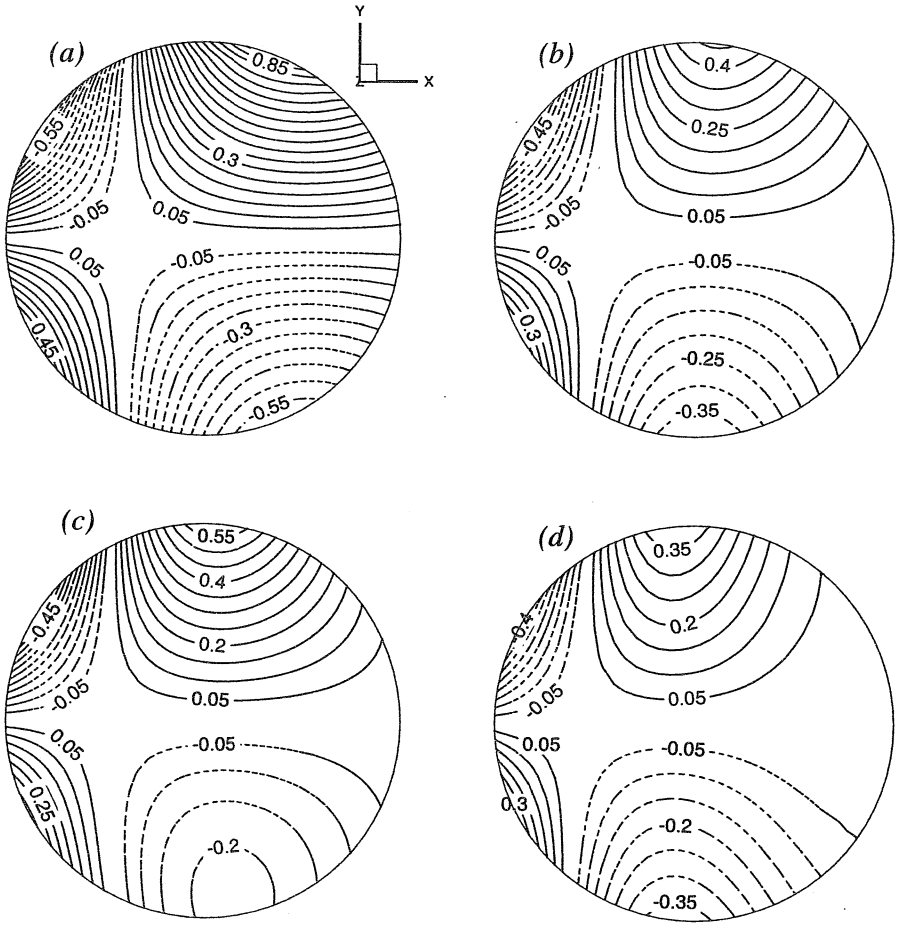

FIGURE 17. Contours of y-component of surface pressure for $\Theta = \pi/4$, $\Phi = 0$. a) $Re = 10$, $s = 0.1$; b) $Re = 50$, $s = 0.05$; c) $Re = 50$, $s = 0.2$; and d) $Re = 300$, $s = 0.1$. Contours are plotted in steps of 0.05. The dashed lines indicate negative values.

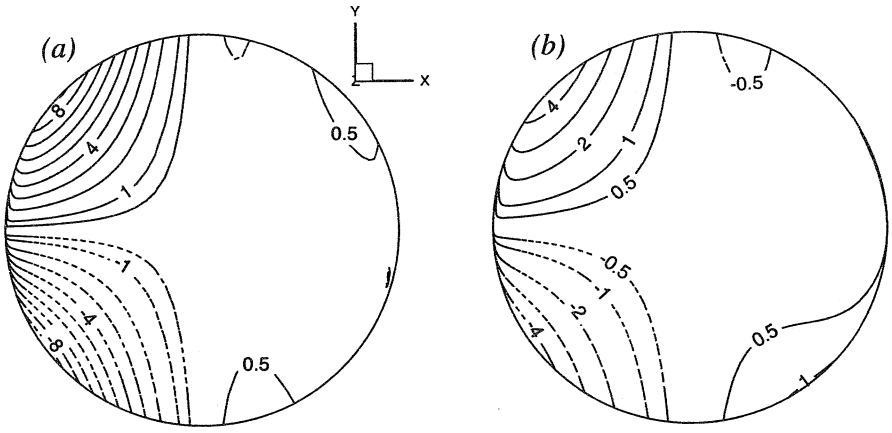

FIGURE 18. Contours of y-component of viscous force due to $\tau_{r\theta}$ contribution. a) $Re = 200, s = 0.1$, b) $Re = 50, s = 0.2$.

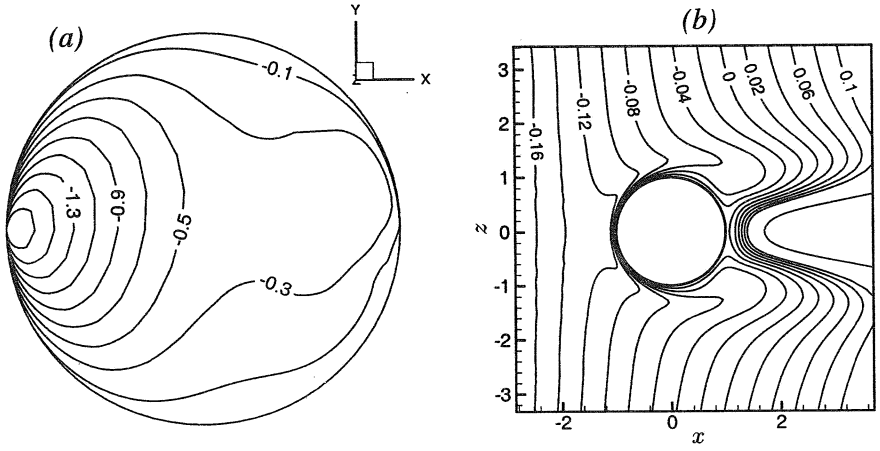

FIGURE 19. Viscous lift due to $\tau_{r\phi}$ at $Re = 200, s = 0.1$. a) Contours of y-component of viscous lift due to $\tau_{r\phi}$, b) Contours of azimuthal velocity component u_ϕ in x-z plane.

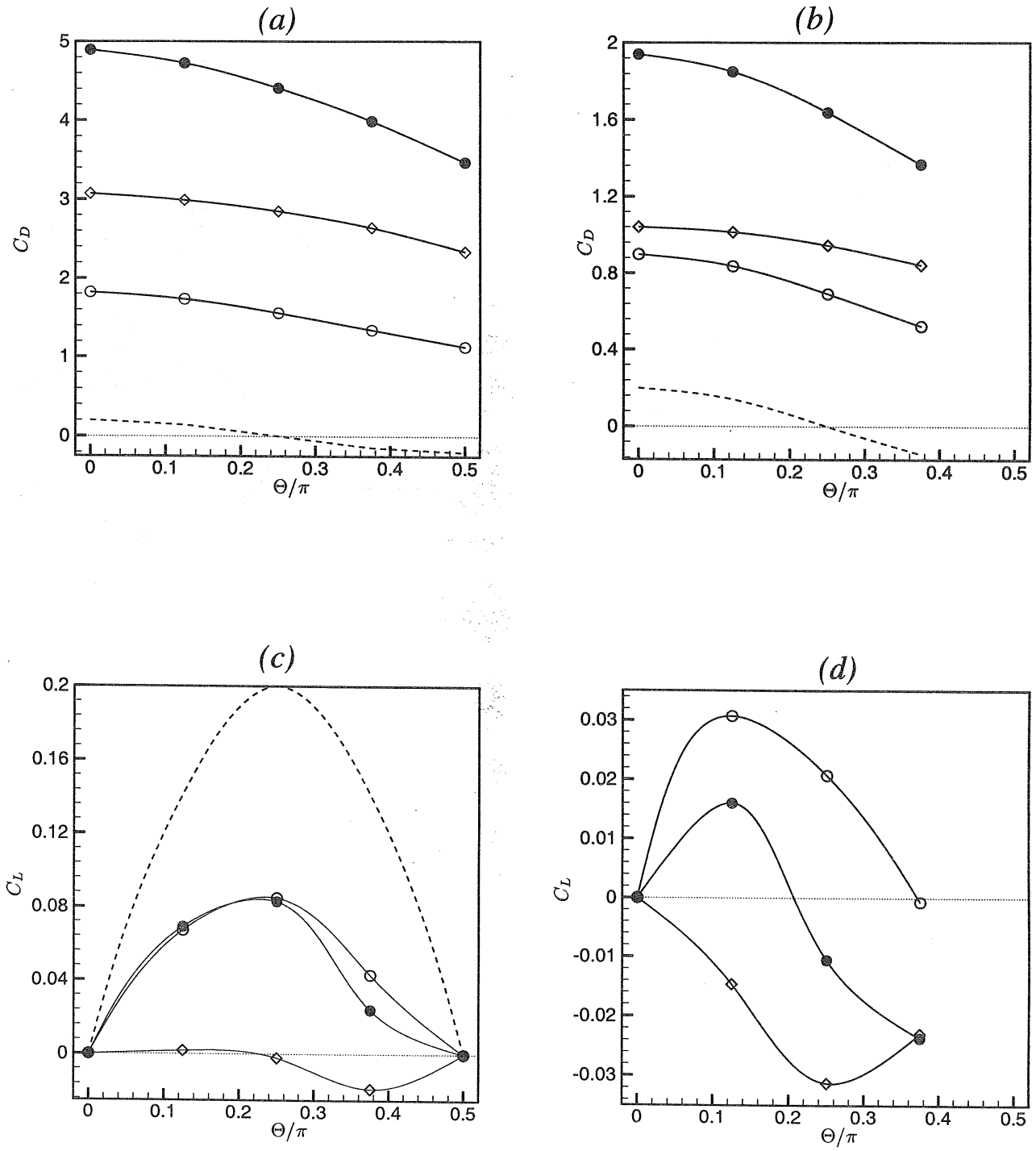

FIGURE 20. Effect of varying Θ on the drag and lift coefficients. Drag coefficients at a) $Re = 10$, $s = 0.1$ and b) $Re = 50$, $s = 0.1$; –●–, C_D; –○–, C_{PD}; –◇–, C_{VD}. Lift coefficients at c) $Re = 10$, $s = 0.1$ and d) $Re = 50$, $s = 0.1$; –●–, C_L; –○–, C_{PL}; –◇–, C_{VL}. - - - -, Potential flow result.

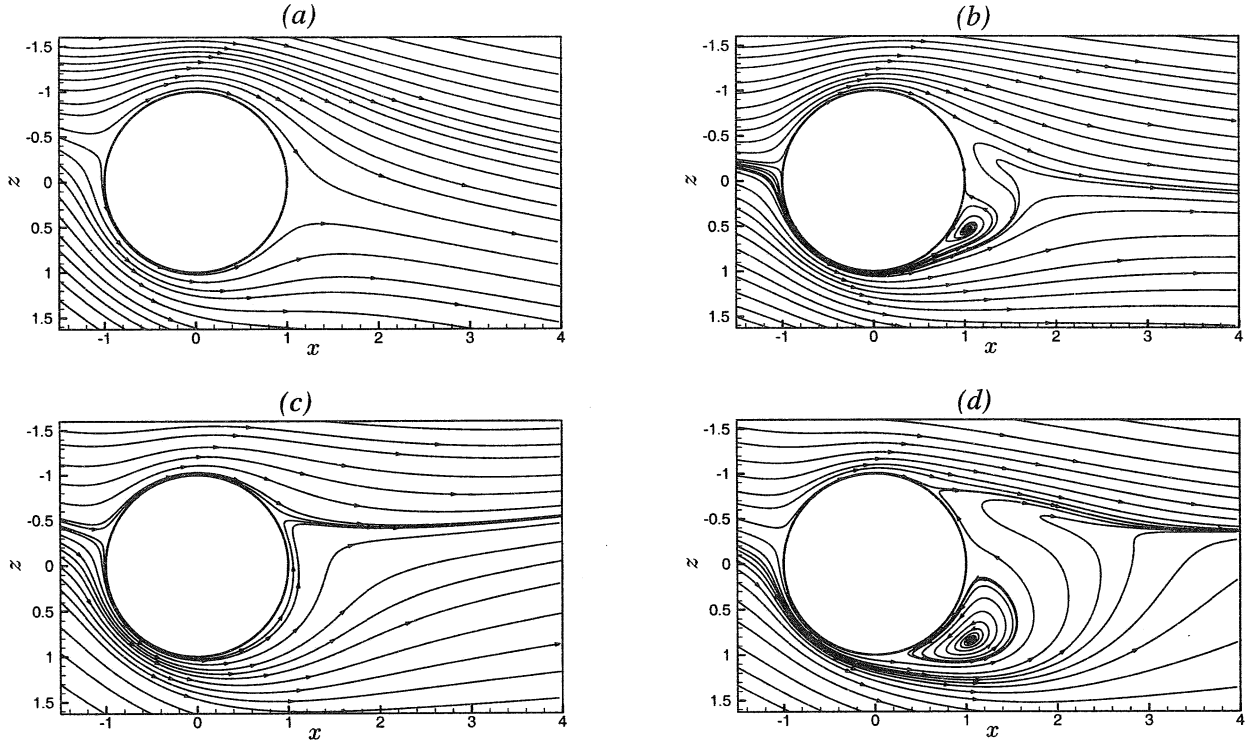

FIGURE 21. Streamline contours for $\Theta = 0, \Phi = 45^0$ on x-z plane. a) $Re = 10, s = 0.1$; b) $Re = 50, s = 0.05$; c) $Re = 50, s = 0.2$; d) $Re = 300, s = 0.1$.

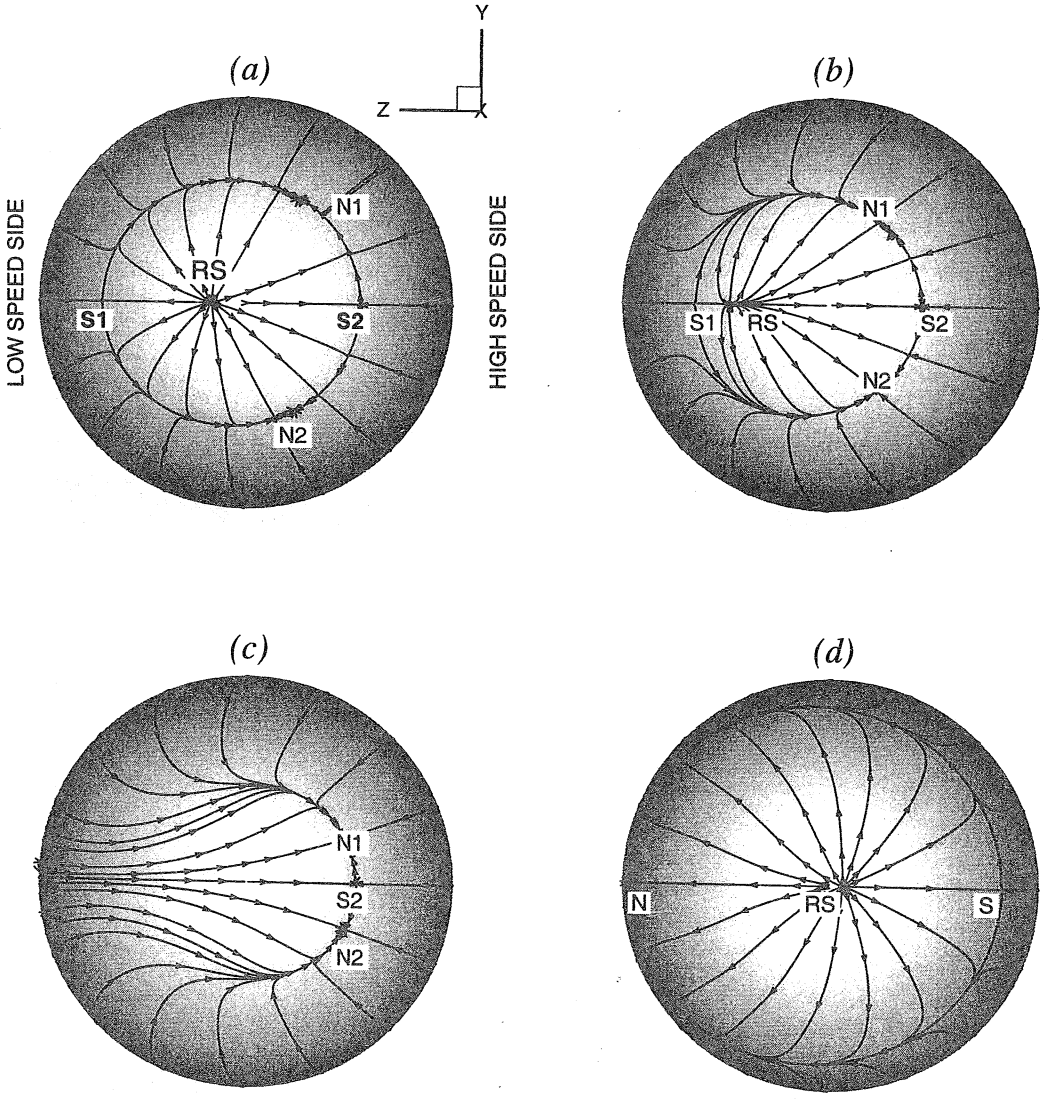

FIGURE 22. Surface streamlines for $\Theta = 0, \Phi = 45^0$: a) $Re = 50, s = 0.05$, b) $Re = 50, s = 0.1$, c) $Re = 50, s = 0.2$, d) $Re = 300, s = 0.1$.

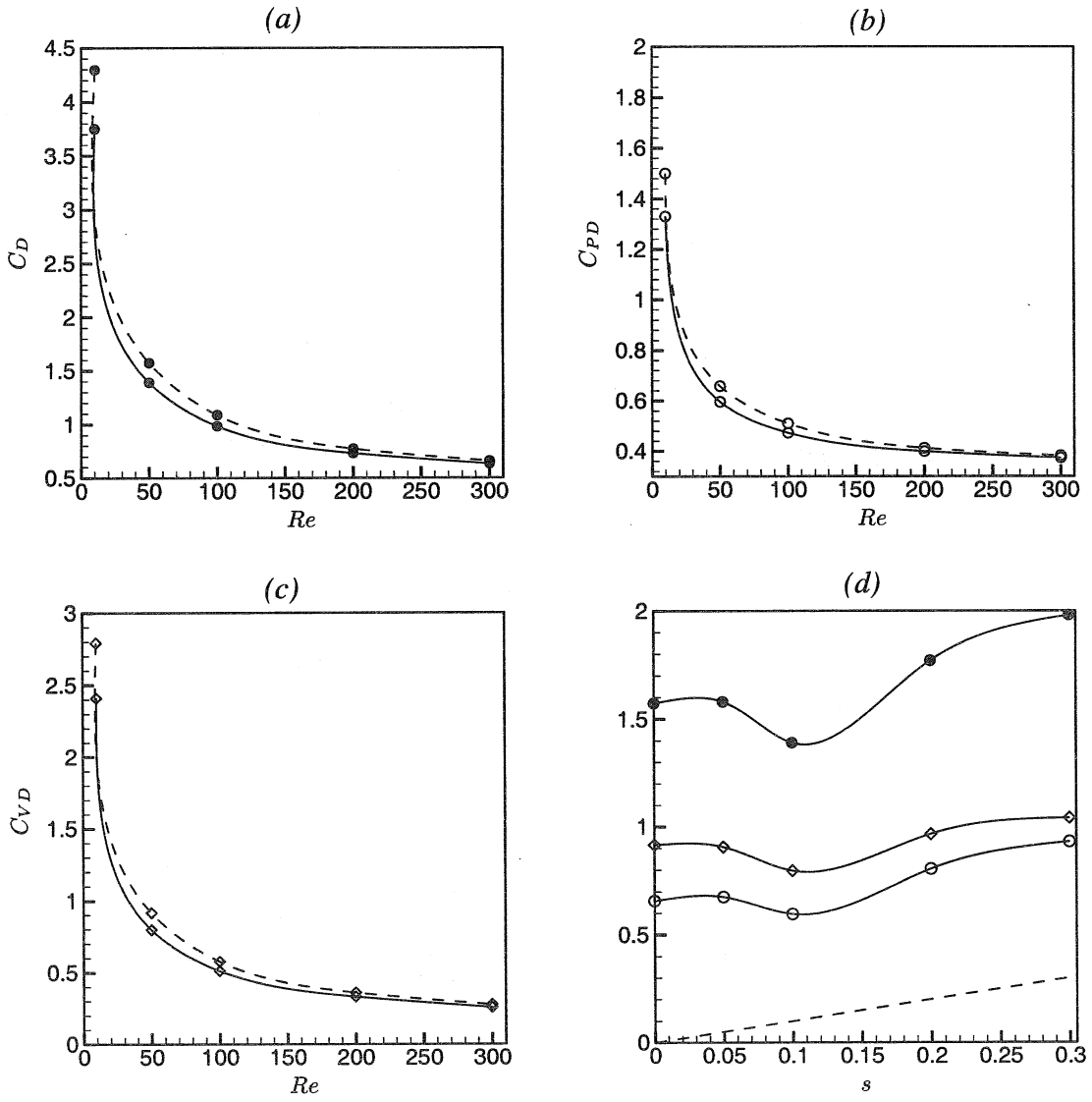

FIGURE 23. Drag coefficients for $\Theta = 0, \Phi = 45^0$. variation of a) C_D, b) C_{PD}, and c) C_{VD} with Re at $s = 0.1$. Dash line is the uniform flow result. d) Drag coefficients at $Re = 50$ and varying s. • C_D; ∘ C_{PD}; ◇ C_{VD}. Dash line is the potential flow result corresponding to $\Theta = 0, \Phi = 45^0$.

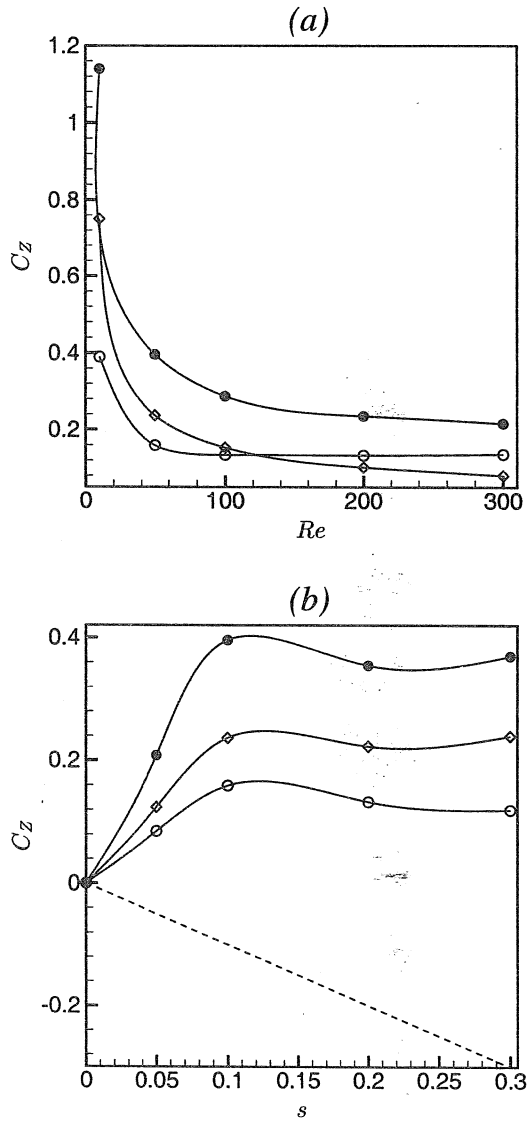

FIGURE 24. Side-force coefficients for $\Theta = 0, \Phi = 45^0$. a) $s = 0.1$, b) $Re = 50$. • C_Z; ∘ $C_{Z,P}$; ◇ $C_{Z,V}$. - - - - - potential flow result.

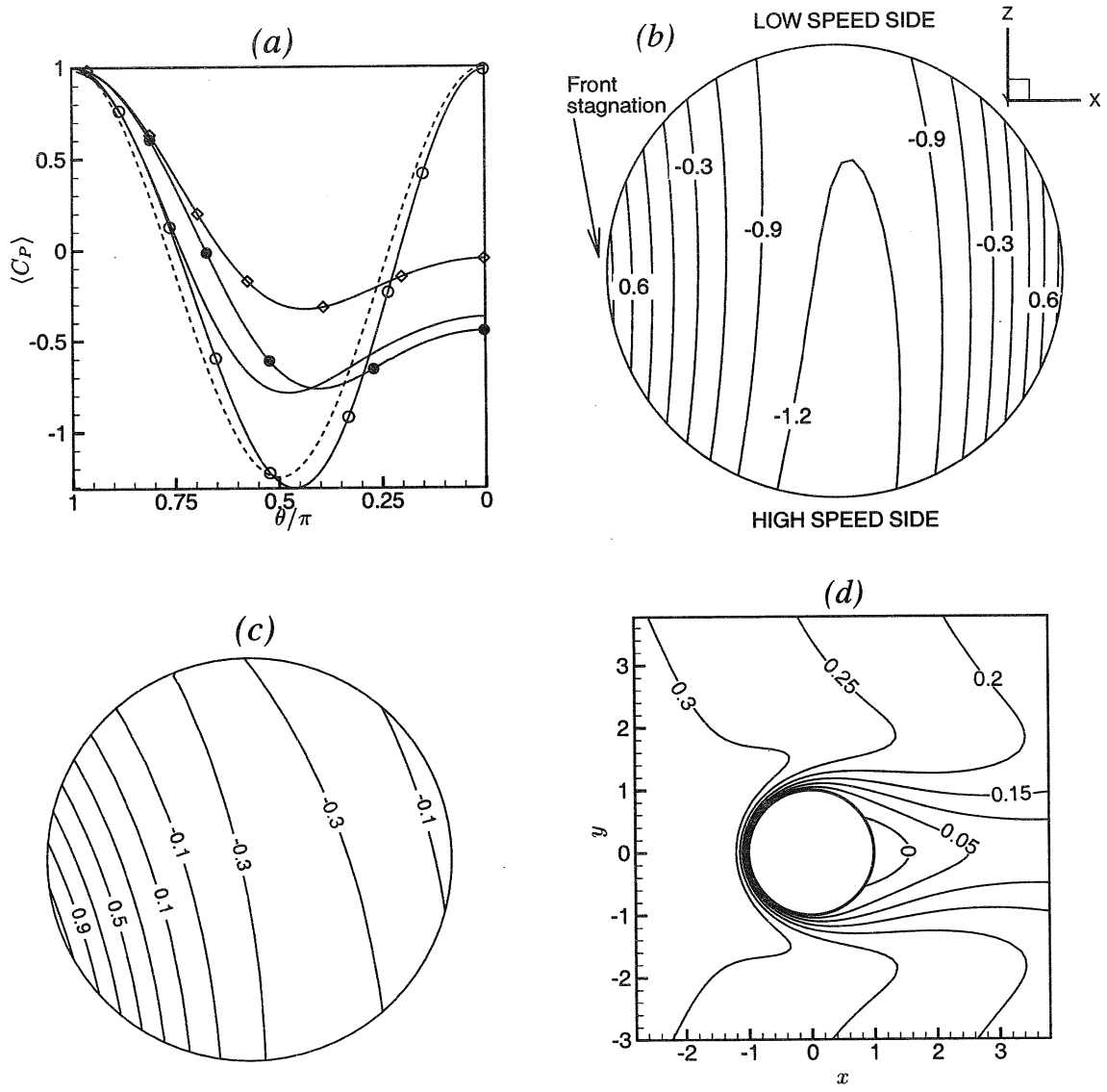

FIGURE 25. $\Theta = 0, \Phi = \pi/4$ case. a) ϕ-averaged surface pressure coefficient : - - - - - potential flow at $s = 0.0$; —○—, potential flow at $s = 0.3$; ———, $Re = 50, s = 0.0$; —◇—, $Re = 50, s = 0.1$; —●—, $Re = 50, s = 0.3$. b) Pressure contours in potential flow at $s = 0.1$. c) Pressure contours for $Re = 50, s = 0.1$. d) Contours of u_ϕ on x-y plane for $Re = 50, s = 0.1$.

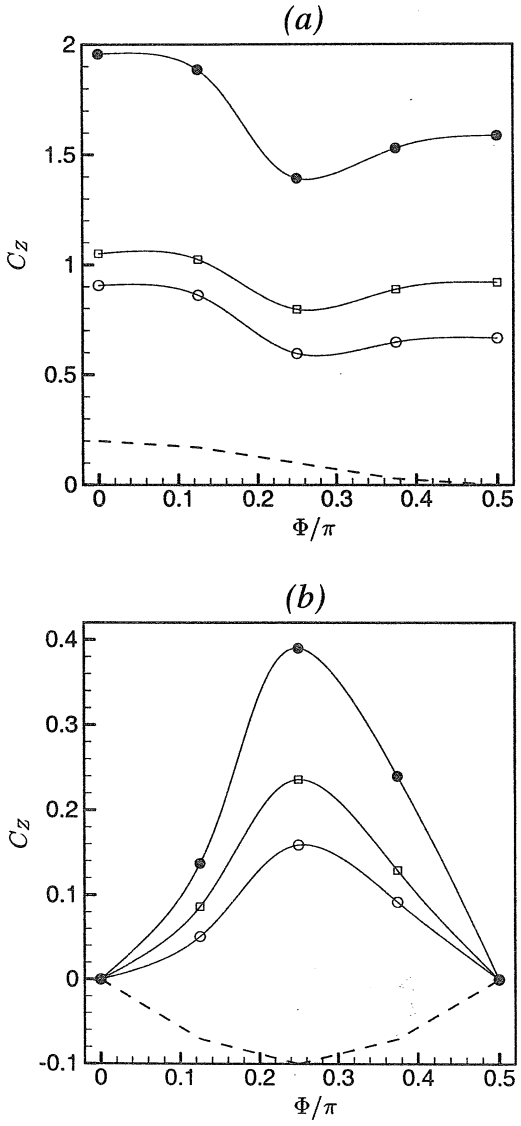

FIGURE 26. Effect of varying Φ. a) Drag coefficients : •, C_D; ○, C_{PD}; ◇, C_{VD}. b) Side-force coefficients : •, C_Z; ○, $C_{Z,P}$; ◇, $C_{Z,V}$. Data corresponds to $Re = 50, s = 0.1$ case. Dash line is the potential flow result at $s = 0.1$.

List of Recent TAM Reports

No.	Authors	Title	Date
847	Keane, R. D., N. Fujisawa, and R. J. Adrian	Unsteady non-penetrative thermal convection from non-uniform surfaces—In *Geophysical and Astrophysical Convection*, R. Kerr, ed. (1997)	Feb. 1997
848	Aref, H., and M. Brøns	On stagnation points and streamline topology in vortex flows—*Journal of Fluid Mechanics* **370**, 1–27 (1998)	Mar. 1997
849	Asghar, S., T. Hayat, and J. G. Harris	Diffraction by a slit in an infinite porous barrier—*Wave Motion*, **30**, 96–104 (1998)	Mar. 1997
850	Shawki, T. G., H. Aref, and J. W. Phillips	Mechanics on the Web—Proceedings of the International Conference on Engineering Education (Aug. 1997, Chicago)	Apr. 1997
851	Stewart, D. S., and J. Yao	The normal detonation shock velocity–curvature relationship for materials with non-ideal equation of state and multiple turning points—*Combustion* **113**, 224–235 (1998)	Apr. 1997
852	Fried, E., A. Q. Shen, and S. T. Thoroddsen	Wave patterns in a thin layer of sand within a rotating horizontal cylinder—*Physics of Fluids* **10**, 10–12 (1998)	Apr. 1997
853	Boyland, P. L., H. Aref, and M. A. Stremler	Topological fluid mechanics of stirring—*Bulletin of the American Physical Society* **41**, 1683 (1996)	Apr. 1997
854	Parker, S. J., and S. Balachandar	Viscous and inviscid instabilities of flow along a streamwise corner—*Bulletin of the American Physical Society* **42**, 2155 (1997)	May 1997
855	Soloff, S. M., R. J. Adrian, and Z.-C. Liu	Distortion compensation for generalized stereoscopic particle image velocimetry—*Measurement Science and Technology* **8**, 1–14 (1997)	May 1997
856	Zhou, Z., R. J. Adrian, S. Balachandar, and T. M. Kendall	Mechanisms for generating coherent packets of hairpin vortices in near-wall turbulence—*Bulletin of the American Physical Society* **42**, 2243 (1997)	June 1997
857	Neishtadt, A. I., D. L. Vainshtein, and A. A. Vasiliev	Chaotic advection in a cubic stokes flow—*Physica D* **111**, 227 (1997).	June 1997
858	Weaver, R. L.	Ultrasonics in an aluminum foam—*Ultrasonics* **36**, 435–442 (1998)	July 1997
859	Riahi, D. N.	High gravity convection in a mushy layer during alloy solidification—In *Nonlinear Instability, Chaos and Turbulence*, D. N. Riahi and L. Debnath, eds., **1**, 301–336 (1998)	July 1997
860	Najjar, F. M., and S. Balachandar	Low-frequency unsteadiness in the wake of a normal plate, *Bulletin of the American Physical Society* **42**, 2212 (1997)	Aug. 1997
861	Short, M.	A parabolic linear evolution equation for cellular detonation instability—*Combustion Theory and Modeling* **1**, 313–346 (1997)	Aug. 1997
862	Short, M., and D. S. Stewart	Cellular detonation stability, I: A normal-mode linear analysis—*Journal of Fluid Mechanics* **368**, 229–262 (1998)	Sept. 1997
863	Carranza, F. L., and R. B. Haber	A numerical study of intergranular fracture and oxygen embrittlement in an elastic–viscoplastic solid—*Journal of the Mechanics and Physics of Solids*, **47**, 27–58 (1997)	Oct. 1997
864	Sakakibara, J., and R. J. Adrian	Whole-field measurement of temperature in water using two-color laser-induced fluorescence—*Experiments in Fluids* **26**, 7–15 (1999)	Oct. 1997
865	Riahi, D. N.	Effect of surface corrugation on convection in a three-dimensional finite box of fluid-saturated porous material—*Theoretical and Computational Fluid Dynamics*, 13, 189-208 (1999)	Oct. 1997
866	Baker, C. F., and D. N. Riahi	Three-dimensional flow instabilities during alloy solidification—*Bulletin of the American Physical Society* **41**, 1699 (1998)	Oct. 1997
867	Fried, E.	Introduction (only) to *The Physical and Mathematical Foundations of the Continuum Theory of Evolving Phase Interfaces* (book containing 14 seminal papers dedicated to Morton E. Gurtin), Berlin: Springer-Verlag, in press (1998)	Oct. 1997
868	Folguera, A., and J. G. Harris	Coupled Rayleigh surface waves in a slowly varying elastic waveguide—*Proceedings of the Royal Society of London A* **455**, 917–931 (1998)	Oct. 1997

List of Recent TAM Reports (cont'd)

No.	Authors	Title	Date
869	Stewart, D. S.	Detonation shock dynamics: Application for precision cutting of metal with detonation waves	Oct. 1997
870	Shrotriya, P., and N. R. Sottos	Creep and relaxation behavior of woven glass/epoxy substrates for multilayer circuit board applications—*Polymer Composites* **19**, 567–578 (1998)	Nov. 1997
871	Riahi, D. N.	Boundary wave–vortex interaction in channel flow at high Reynolds numbers, *Fluid Dynamics Research* **25**, 129–145 (1999)	Nov. 1997
872	George, W. K., L. Castillo, and M. Wosnik	A theory for turbulent pipe and channel flows—paper presented at *Disquisitiones Mechanicae* (Urbana, Ill., October 1996)	Nov. 1997
873	Aslam, T. D., and D. S. Stewart	Detonation shock dynamics and comparisons with direct numerical simulation—*Combustion Theory and Modeling* **3**, 77–101 (1999)	Dec. 1997
874	Short, M., and A. K. Kapila	Blow-up in semilinear parabolic equations with weak diffusion *Combustion Theory and Modeling* **2**, 283-291 (1998)	Dec. 1997
875	Riahi, D. N.	Analysis and modeling for a turbulent convective plume—*Mathematical and Computer Modeling* **28**, 57–63 (1998)	Jan. 1998
876	Stremler, M. A., and H. Aref	Motion of three point vortices in a periodic parallelogram—*Journal of Fluid Mechanics* **392**, 101-128 (1999)	Feb. 1998
877	Dey, N., K. J. Hsia, and D. F. Socie	On the stress dependence of high-temperature static fatigue life of ceramics	Feb. 1998
878	Brown, E. N., and N. R. Sottos	Thermoelastic properties of plain weave composites for multilayer circuit board applications	Feb. 1998
879	Riahi, D. N.	On the effect of a corrugated boundary on convective motion—*Journal of Theoretical and Applied Mechanics*, in press (1999)	Feb. 1998
880	Riahi, D. N.	On a turbulent boundary layer flow over a moving wavy wall	Mar. 1998
881	Riahi, D. N.	Vortex formation and stability analysis for shear flows over combined spatially and temporally structured walls—*Mathematical Problems in Engineering* **5**, 317–328 (1999)	June 1998
882	Short, M., and D. S. Stewart	The multi-dimensional stability of weak heat release detonations—*Journal of Fluid Mechanics* **382**, 109–135 (1999)	June 1998
883	Fried, E., and M. E. Gurtin	Coherent solid-state phase transitions with atomic diffusion: A thermomechanical treatment—*Journal of Statistical Physics* **95**, 1361–1427 (1999)	June 1998
884	Langford, J. A., and R. D. Moser	Optimal large-eddy simulation formulations for isotropic turbulence—*Journal of Fluid Mechanics* **398**, 321–346 (1999)	July 1998
885	Riahi, D. N.	Boundary-layer theory of magnetohydrodynamic turbulent convection—*Proceedings of the Indian National Academy (Physical Science)* **65A**, 109–116 (1999)	Aug. 1998
886	Riahi, D. N.	Nonlinear thermal instability in spherical shells—in *Nonlinear Instability, Chaos and Turbulence* **2**, 377–402 (1999)	Aug. 1998
887	Riahi, D. N.	Effects of rotation on fully non-axisymmetric chimney convection during alloy solidification—*Journal of Crystal Growth* **204**, 382–394 (1999)	Sept. 1998
888	Fried, E., and S. Sellers	The Debye theory of rotary diffusion	Sept. 1998
889	Short, M., A. K. Kapila, and J. J. Quirk	The hydrodynamic mechanisms of pulsating detonation wave instability—*Proceedings of the Royal Society of London, A* **357**, 3621–3638 (1999)	Sept. 1998
890	Stewart, D. S.	The shock dynamics of multidimensional condensed and gas phase detonations—Proceedings of the 27th International Symposium on Combustion (Boulder, Colo.)	Sept. 1998
891	Kim, K. C., and R. J. Adrian	Very large-scale motion in the outer layer—*Physics of Fluids* **2**, 417–422 (1999)	Oct. 1998
892	Fujisawa, N., and R. J. Adrian	Three-dimensional temperature measurement in turbulent thermal convection by extended range scanning liquid crystal thermometry—*Journal of Visualization* **1**, 355-364 (1999)	Oct. 1998

List of Recent TAM Reports (cont'd)

No.	*Authors*	*Title*	*Date*
893	Shen, A. Q., E. Fried, and S. T. Thoroddsen	Is segregation-by-particle-type a generic mechanism underlying finger formation at fronts of flowing granular media?—*Particulate Science and Technology* **17**, 141–148 (1999)	Oct. 1998
894	Shen, A. Q.	Mathematical and analog modeling of lava dome growth	Oct. 1998
895	Buckmaster, J. D., and M. Short	Cellular instabilities, sub-limit structures, and edge-flames in premixed counterflows—*Combustion Theory and Modeling* **3**, 199–214 (1999)	Oct. 1998
896	Harris, J. G.	*Elastic waves*—Part of a book to be published by Cambridge University Press	Dec. 1998
897	Paris, A. J., and G. A. Costello	Cord composite cylindrical shells	Dec. 1998
898	Students in TAM 293–294	Thirty-fourth student symposium on engineering mechanics (May 1997), J. W. Phillips, coordinator: Selected senior projects by M. R. Bracki, A. K. Davis, J. A. (Myers) Hommema, and P. D. Pattillo	Dec. 1998
899	Taha, A., and P. Sofronis	A micromechanics approach to the study of hydrogen transport and embrittlement	Jan. 1999
900	Ferney, B. D., and K. J. Hsia	The influence of multiple slip systems on the brittle–ductile transition in silicon—*Materials Science Engineering A* **272**, 422–430 (1999)	Feb. 1999
901	Fried, E., and A. Q. Shen	Supplemental relations at a phase interface across which the velocity and temperature jump	Mar. 1999
902	Paris, A. J., and G. A. Costello	Cord composite cylindrical shells: Multiple layers of cords at various angles to the shell axis	Apr. 1999
903	Ferney, B. D., M. R. DeVary, K. J. Hsia, and A. Needleman	Oscillatory crack growth in glass—*Scripta Materialia* **41**, 275–281 (1999)	Apr. 1999
904	Fried, E., and S. Sellers	Microforces and the theory of solute transport	Apr. 1999
905	Balachandar, S., J. D. Buckmaster, and M. Short	The generation of axial vorticity in solid-propellant rocket-motor flows	May 1999
906	Aref, H., and D. L. Vainchtein	The equation of state of a foam	May 1999
907	Subramanian, S. J., and P. Sofronis	Modeling of the interaction between densification mechanisms in powder compaction	May 1999
908	Aref, H., and M. A. Stremler	Four-vortex motion with zero total circulation and impulse—*Physics of Fluids* **11**, 3704-3715	May 1999
909	Adrian, R. J., K. T. Christensen, and Z.-C. Liu	On the analysis and interpretation of turbulent velocity fields—*Experiments in Fluids*, in press (1999)	May 1999
910	Fried, E., and S. Sellers	Theory for atomic diffusion on fixed and deformable crystal lattices	June 1999
911	Sofronis, P., and N. Aravas	Hydrogen induced shear localization of the plastic flow in metals and alloys	June 1999
912	Anderson, D. R., D. E. Carlson, and E. Fried	A continuum-mechanical theory for nematic elastomers	June 1999
913	Riahi, D. N.	High Rayleigh number convection in a rotating melt during alloy solidification—*Recent Developments in Crystal Growth Research*, in press (2000)	July 1999
914	Riahi, D. N.	Buoyancy driven flow in a rotating low Prandtl number melt during alloy solidification—*Current Topics in Crystal Growth Research*, in press (2000)	July 1999
915	Adrian, R. J.	On the physical space equation for large-eddy simulation of inhomogeneous turbulence	July 1999

List of Recent TAM Reports (cont'd)

No.	*Authors*	*Title*	*Date*
916	Riahi, D. N.	Wave and vortex generation and interaction in turbulent channel flow between wavy boundaries	July 1999
917	Boyland, P. L., M. A. Stremler, and H. Aref	Topological fluid mechanics of point vortex motions	July 1999
918	Riahi, D. N.	Effects of a vertical magnetic field on chimney convection in a mushy layer—*Journal of Crystal Growth*, in press (2000)	Aug. 1999
919	Riahi, D. N.	Boundary mode–vortex interaction in turbulent channel flow over a non-wavy rough wall	Sept. 1999
920	Block, G. I., J. G. Harris, and T. Hayat	Measurement models for ultrasonic nondestructive evaluation	Sept. 1999
921	Zhang, S., and K. J. Hsia	Modeling the fracture of a sandwich structure due to cavitation in a ductile adhesive layer	Sept. 1999
922	Nimmagadda, P. B. R., and P. Sofronis	Leading order asymptotics at sharp fiber corners in creeping-matrix composite materials	Oct. 1999
923	Yoo, S., and D. N. Riahi	Effects of a moving wavy boundary on channel flow instabilities	Nov. 1999
924	Adrian, R. J., C. D. Meinhart, and C. D. Tomkins	Vortex organization in the outer region of the turbulent boundary layer	Nov. 1999
925	Riahi, D. N., and A. T. Hsui	Finite amplitude thermal convection with variable gravity	Dec. 1999
926	Kwok, W. Y., R. D. Moser, and J. Jiménez	A critical evaluation of the resolution properties of *B*-spline and compact finite difference methods	Feb. 2000
927	Ferry, J. P., and S. Balachandar	A fast Eulerian method for two-phase flow	Feb. 2000
928	Thoroddsen, S. T., and K. Takehara	The coalescence–cascade of a drop	Feb. 2000
929	Liu, Z.-C., R. J. Adrian, and T. J. Hanratty	Large-scale modes of turbulent channel flow: Transport and structure	Feb. 2000
930	Borodai, S. G., and R. D. Moser	The numerical decomposition of turbulent fluctuations in a compressible boundary layer	Mar. 2000
931	Balachandar, S., and F. M. Najjar	Optimal two-dimensional models for wake flows	Mar. 2000
932	Yoon, H. S., K. V. Sharp, D. F. Hill, R. J. Adrian, S. Balachandar, M. Y. Ha, and K. Kar	Integrated experimental and computational approach to simulation of flow in a stirred tank	Mar. 2000
933	Sakakibara, J., Hishida, K., and W. R. C. Phillips	On the vortical structure in a plane impinging jet	Apr. 2000
934	Phillips, W. R. C.	Eulerian space–time correlations in turbulent shear flows	Apr. 2000
935	Hsui, A. T., and D. N. Riahi	Onset of thermal–chemical convection with crystallization within a binary fluid and its geological implications	Apr. 2000
936	Cermelli, P., E. Fried, and S. Sellers	Configurational stress, yield, and flow in rate-independent plasticity	Apr. 2000
937	Adrian, R. J., C. Meneveau, R. D. Moser, and J. J. Riley	Final report on 'Turbulence Measurements for LES' workshop	Apr. 2000
938	Bagchi, P., and S. Balachandar	Linearly varying ambient flow past a sphere at finite Reynolds number—Part 1: Wake structure and forces in steady straining flow	Apr. 2000